Full-bandwidth anisotropic Migdal-Eliashberg theory and its application to superhydrides

Roman Lucrezi,[1, *] Pedro P. Ferreira,[1, 2, *] Samad Hajinazar,[3, 4]

Hitoshi Mori,[3] Hari Paudyal,[3] Elena R. Margine,[3, †] and Christoph Heil[1, ‡]

[1]*Institute of Theoretical and Computational Physics, Graz University of Technology, NAWI Graz, 8010, Graz, Austria*

[2]*Universidade de São Paulo, Escola de Engenharia de Lorena, DEMAR, Lorena, Brazil*

[3]*Department of Physics, Applied Physics, and Astronomy,*
Binghamton University-SUNY, Binghamton, New York 13902, USA

[4]*Present address: Department of Chemistry, University at Buffalo, Buffalo, NY 14260, USA*

(Dated: January 15, 2024)

Abstract: Migdal-Eliashberg theory is one of the state-of-the-art methods for describing conventional superconductors from first principles. However, widely used implementations assume a constant density of states around the Fermi level, which hinders a proper description of materials with distinct features in its vicinity. Here, we present an implementation of the Migdal-Eliashberg theory within the EPW code that considers the full electronic structure and accommodates scattering processes beyond the Fermi surface. To significantly reduce computational costs, we introduce a non-uniform sampling scheme along the imaginary axis. We demonstrate the power of our implementation by applying it to the sodalite-like clathrates YH_6 and CaH_6, and to the covalently-bonded H_3S and D_3S. Furthermore, we investigate the effect of maximizing the density of states at the Fermi level in doped H_3S and $BaSiH_8$ within the full-bandwidth treatment compared to the constant-density-of-states approximation. Our findings highlight the importance of this advanced treatment in such complex materials.

INTRODUCTION

Discovering and designing new and technologically relevant superconductors is one of the grand challenges of modern science [1]. Conventional superconductivity arises from an intricate interplay between the electrons and the vibrational modes of the lattice, which can be condensed into a single parameter known as the electron-phonon (el-ph) coupling strength λ. This interaction leads to pairing electrons with opposing spins below the critical temperature T_c, creating an energy gap at the Fermi surface and resulting in a zero-resistance superconducting condensate. Since the pioneering work of Bardeen, Cooper, and Schrieffer (BCS) [2], advancements in computational and theoretical techniques have allowed accurate calculations of λ and fully ab-initio predictions of T_c [3]. The density-functional theory for superconductors [4–6] and the anisotropic Migdal-Eliashberg theory (AME) [7, 8] are state-of-the-art examples of such techniques that have contributed significantly in unraveling the properties of the superconducting states of seminal materials like MgB_2 [9–11] and NbS_2 [12] in unprecedented detail, and in predicting entirely novel classes of superconductors from first principles [13]. One of the most topical examples is the class of the high-pressure superhydrides [14–16], which have revolutionized the search for high-T_c superconductivity by demonstrating that detailed calculations of the electronic structure, phonon dispersion, and el-ph coupling can guide experiments in the search for new superconducting materials. Prominent examples would be LaH_{10}, theoretically predicted in 2017 [17, 18] and experimentally confirmed two years later [19], YH_6 [20–23] and CaH_6 [24–26], or most recently, $LaBeH_8$, the first successfully synthesized ternary superhydride [27, 28].

The AME formalism is particularly useful in describing the order parameter of weak and strong coupling su-

perconductors. However, computing the el-ph matrix elements and numerically solving the Eliashberg equations requires extremely dense electron and phonon meshes in the Brillouin zone (BZ) to overcome the strong sensitivity to the sampling of the el-ph scattering processes involving states around the Fermi level [29]. The AME implementation of the EPW code [30, 31], which was developed by some of the present authors [32], enables the interpolation of a small number of el-ph matrix elements to arbitrary electron and phonon wave vectors in the Bloch representation using maximally localized Wannier functions [33]. This has helped to bridge the gap between experiments and theory and has been widely used in the last few years to determine, among other superconducting properties, the momentum- and band-resolved superconducting order parameter of various anisotropic bulk materials [34–38], layered compounds [39–41], and two-dimensional systems [42–46].

Despite the extraordinary success of the AME implementation in EPW, its main shortage comes from the assumption that the density of states (DOS) is constant for a finite energy window around the Fermi level ε_F (of the order of the Debye energies) where the superconducting coupling occurs [32]. This approximation, widely employed in literature, is valid for a broad range of compounds but will break down for materials with narrow bands or critical points in the vicinity of ε_F [47, 48], such as van Hove singularities (VHSs) and Lifshitz transitions.

With the present work, we remedy this shortcoming. Our implementation goes beyond the limitations of the previous approach, by explicitly incorporating scattering processes of electrons with energies and momenta beyond the confines of the Fermi surface. This is made possible through the self-consistent determination of the mass renormalization function, energy shift, and order parameter at every temperature while ensuring the system's charge neutrality (see Supplemen-

tary Method 1). The corresponding theoretical considerations and equations are detailed in the methods section and in Supplementary Method 1. As this leads to an increased computational workload, we have also implemented a sparse, non-uniform sampling scheme over the imaginary axis, considerably lowering the number of Matsubara frequencies needed compared to the uniform sampling scheme, which, in practice, highly decreases the computational costs (see methods section).

We apply this implementation to two different classes of topical superhydrides, the sodalite-like clathrates YH_6 and CaH_6, and the covalently-bonded H_3S and D_3S. Results and discussion are provided under *General applications and benchmarking* and material-specific computational details can be found in the methods section. Moreover, we present compelling evidence that the commonly used approach of computationally optimizing T_c by maximizing the DOS at ε_F ($N(\varepsilon_F)$) is often ineffective, as the reported enhancements in T_c are, in fact, artifacts resulting from the constant-DOS approximation. To support this claim, we conduct a detailed study of electron- and hole-doping effects in H_3S and $BaSiH_8$ using our full-bandwidth implementation (see *Application to doped hydrides*). The results shed light on the limitations of the maximizing-$N(\varepsilon_F)$ strategy, emphasizing the need for a more comprehensive and accurate approach in predicting superconducting properties, as provided with our implementation.

RESULTS

General applications and benchmarking

The emergence of superconductivity at record-breaking temperatures has reignited the hope of achieving superconductivity at ambient conditions [1]. Indeed, the discoveries of near-room temperature superconductivity in H_3S [49, 50] and LaH_{10} [18, 19, 51] at megabar pressures constitute a new landmark for superconductivity and for the prediction of entirely new materials with advanced functionalities fully ab-initio.

Among the numerous already predicted and experimentally confirmed superhydrides, H_3S and D_3S have received particular attention from the scientific community. Multiple independent experimental groups employing different characterization techniques have confirmed the existence of the cubic $Im\bar{3}m$-H_3S structure at pressures around 100-200 GPa and its superconducting state near room temperature [52–59]. Furthermore, after the prediction of stable body-centered cubic structures of hydrogen that form sodalite-like cages containing Ca [20] and Y [24] atoms above 150 GPa, YH_6 and CaH_6 have also been comprehensively studied by many independent theoretical [17, 18, 60, 61] and experimental groups [21–23, 25, 26], paving the way for the search for the holy grail of superconductivity [27, 37, 62–64]. Many hydrides exhibit interesting features, such as van Hove singularities near ε_F and metallic hydrogen states with strong el-ph

coupling [1], which make them a unique condensed matter platform to study superconductivity.

Due to their topical relevance and the amount of experimental data available, we have employed the full-bandwidth method to the sodalite-like clathrates YH_6 and CaH_6, and to the covalently-bonded H_3S and D_3S. In the following, we will consider two levels of approximation when solving the AME. The first is the Fermi-surface-restricted approximation (FSR) [30], which, as discussed in detail in the methods section, assumes that the DOS around ε_F is constant. The second, and main object of interest in this work, is the full-bandwidth method (FBW), which takes into account the full energy dependence of the DOS and thus allows for the inclusion of el-ph scattering processes away from ε_F [31].

Furthermore, our implementation of FBW comes in two different flavors: (*i*) updating the chemical potential, μ, while solving self-consistently the AME equations to maintain the charge neutrality of the system (referred to as FBW+μ henceforth); and (*ii*) keeping the chemical potential fixed (referred to simply as FBW) to lighten the computational load. We will also compare our results for T_c to the values given by the commonly employed semi-empirical modified McMillan equation [65, 66] and the recently proposed machine-learned SISSO model [67].

YH_6 and CaH_6

To benchmark our implementation, we first take a look at YH_6 and CaH_6, two hydrides whose variation in the DOS around ε_F is rather small, i.e., they are materials for which the FSR approach should be reasonably accurate.

In the following, we summarize the important physical properties to understand the emergence of a high-T_c in these materials: The electronic band structures and DOS for YH_6 and CaH_6 at a pressure of 200 GPa are presented in Figs. 1(**a**) and (**d**). The corresponding phonon dispersions and phonon DOS along with the isotropic Eliashberg spectral function $\alpha^2F(\omega)$ and the cumulative el-ph coupling strength $\lambda(\omega)$ are reported in Figs. 1(**b**) and (**e**). The relatively high el-ph coupling is associated primarily with the Kohn anomalies observed in the phonon dispersion along the Γ–H direction for YH_6 and the H–N direction for CaH_6 [24]. For YH_6, numerous modes between 90 meV and 220 meV significantly contribute to the total el-ph coupling strength. Conversely, the primary contribution for CaH_6 is localized in the energy range of 100-160 meV, derived from the T_{2g} and the E_g modes at the Γ-zone center belonging to the vibrations of the H_4 units [20]. By integrating $\alpha^2F(\omega)$, the total el-ph coupling strengths for both YH_6 and CaH_6 are close to 2.0. This value and the $\alpha^2F(\omega)$ functions are in excellent agreement with the calculations presented in Refs. [20, 60].

Figures 1(**c**) and (**f**) depict the anisotropic superconducting gap $\Delta_{n\mathbf{k}}$ as a function of temperature for YH_6 and CaH_6 at 200 GPa using the FSR, FBW, and FBW+μ implementations, with $\mu^* = 0.16$. YH_6 exhibits two well-defined super-
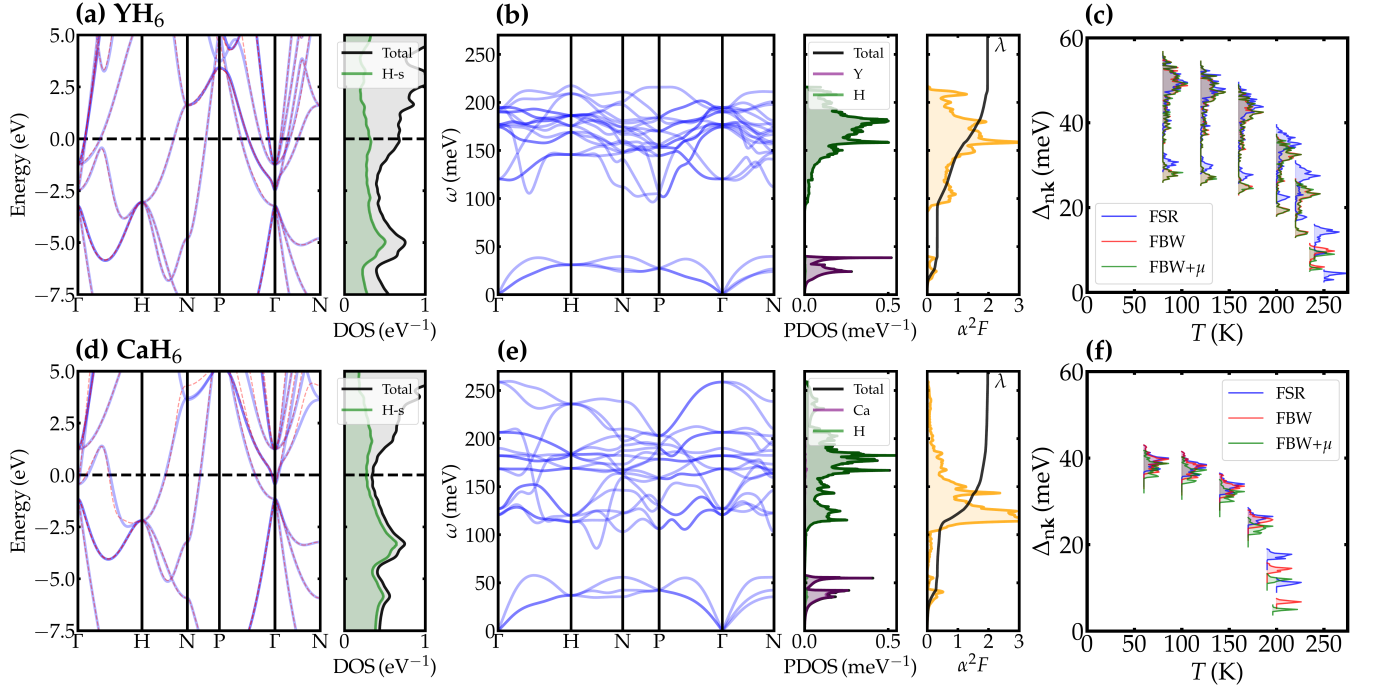
Figure 1. **Electron, phonon, and superconducting properties for sodalite-like clathrates:** Panel **(a)** shows the calculated electronic band structure and DOS with respect to the Fermi energy ε_F for YH$_6$ at 200 GPa. The solid blue lines represent the DFT bands, the dashed red lines the Wannier bands, the solid black line the total DOS, the shaded green area the projected DOS for hydrogen s states (H-s), and the dashed black line indicates ε_F. Panel **(b)** shows the phonon dispersion (solid blue), the phonon density of states (PDOS, solid black) and its elemental contributions (shaded green and purple), the isotropic Eliashberg spectral function $\alpha^2F(\omega)$ (shaded ochre), and the cumulative electron-phonon coupling parameter $\lambda(\omega)$ (solid black). Panel **(c)** displays the distribution of the values of the anisotropic superconducting gap Δ_{nk} on the Fermi surface according to the FSR (blue), FBW (red), and FBW+μ (green) implementations for the Migdal-Eliashberg equations. Panels **(d)**-**(f)** show the corresponding results for CaH$_6$ at 200 GPa.

conducting gaps on the Fermi surface; a larger, broad energy gap ranging from 35 meV to 56 meV at low temperatures, and a smaller gap at approximately 28 meV, the latter originated from the small zone-centered Fermi surface pockets [12]. The gaps of YH$_6$ close at $T_c \approx 250$ K within the FSR approximation and at $T_c \approx 238$ K within the FBW approach, independent of whether the chemical potential is updated self-consistently or not. CaH$_6$ is a single-gap superconductor featuring a well-defined gap energy with a maximum of approximately 45 meV and broadness of about 5 meV; the T_c value is around 200 K in all three implementations, FSR, FBW, and FBW+μ.

Experimentally, the critical temperature of YH$_6$ varies depending on the synthesis route. Maximum values for T_c ranging from 220 K at 183 GPa [21] to 224 K at 166 GPa [23] have been reported. In contrast, CaH$_6$ exhibits a wider transition width of approximately 25 K, with an onset T_c of 195 K at 185 GPa [25]. A maximum T_c of 215 K for CaH$_6$ has been observed at 172 GPa [26]. At 200 GPa experiments report a T_c of about 211 K for YH$_6$ and about 204 K for CaH$_6$. Considering the considerable variation of T_c with respect to different samples and the uncertainties for a particular measurement, the agreement between experimental values and our numerically determined ones is quite satisfactory. We expect that by in-

cluding corrections from quantum anharmonic effects, which can be sizeable in hydrides [68–70], the difference between experiment and theory could be even further reduced, which will be a topic of future investigation.

As mentioned before, both YH$_6$ and CaH$_6$ exhibit a slowly varying DOS around ε_F and in such cases, the FSR approximation is reasonable for describing the el-ph scattering process around the Fermi level. This is also evident from the fact that the chemical potential remains almost constant throughout the self-consistent solution within FBW+μ. Nevertheless, it is important to note that the FBW implementation offers a better agreement with experiments even for these simple cases.

H_3S and D_3S

In contrast to the XH$_6$ materials described above, the behavior of the DOS around ε_F is quite different in the covalently bonded H$_3$S and D$_3$S hydrides. As indicated in Fig. 2**(a)**, the Fermi level is located right at the shoulder of a marked peak in the DOS, which will give rise to considerable differences between the FSR and FBW approaches.
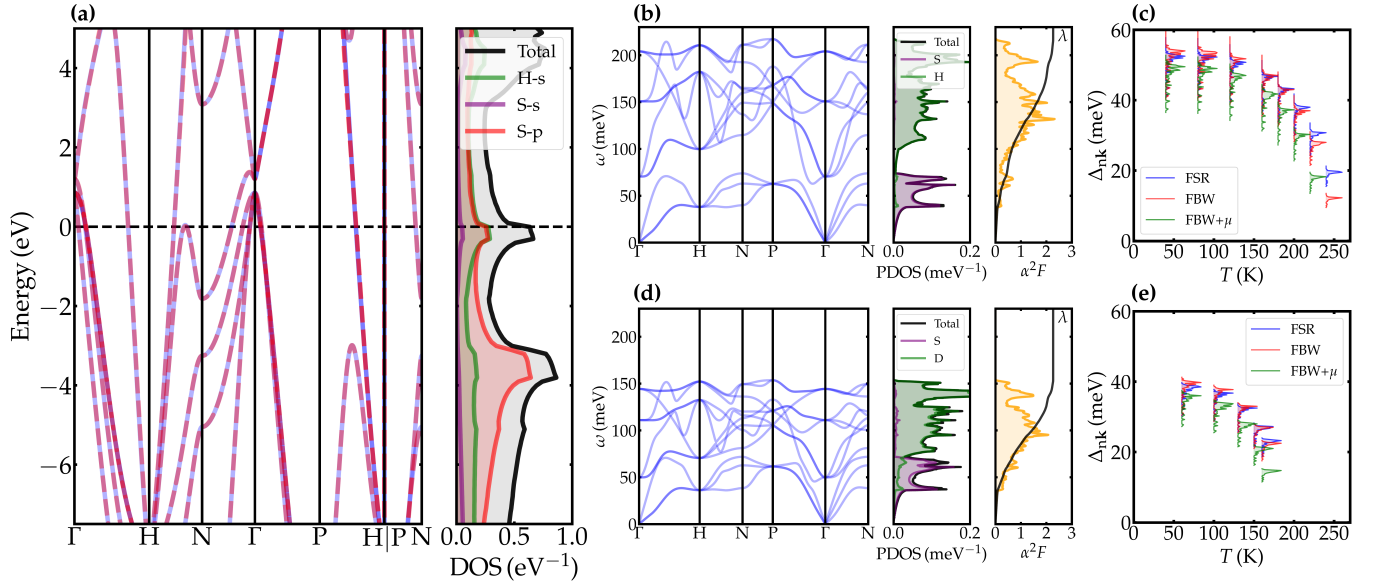
Figure 2. **Electron, phonon, and superconducting properties for the covalently-bonded materials:** Panel **(a)** shows the calculated electronic band structure and DOS with respect to the Fermi energy ε_F for H_3S and D_3S at 200 GPa. The solid blue lines represent the DFT bands, the dashed red lines the Wannier bands, the solid black line the total DOS, the shaded coloured areas the projected DOS for hydrogen s (H-s) and sulfur s and p states (S-s, S-p), and the dashed black line indicates ε_F. Panel **(b)** shows the phonon dispersion (solid blue), the phonon density of states (PDOS, solid black) and its elemental contributions (shaded green and purple), the isotropic Eliashberg spectral function $\alpha^2F(\omega)$ (shaded ochre), and the cumulative electron-phonon coupling parameter $\lambda(\omega)$ (solid black). Panel **(c)** displays the distribution of the values of the anisotropic superconducting gap Δ_{nk} on the Fermi surface according to the FSR (blue), FBW (red), and FBW+μ (green) implementations for the Migdal-Eliashberg equations. Panels **(d)** and **(e)** show the corresponding results for D_3S at 200 GPa.

Figures 2**(b)** and **(d)** report the phonon dispersion, the phonon DOS, $\alpha^2F(\omega)$, and the cumulative $\lambda(\omega)$ for H_3S and D_3S at a pressure of 200 GPa. The corresponding $\alpha^2F(\omega)$ functions possess two main peaks in both compounds. For H_3S, the dominant one is centered around 120 meV, and the second one, less intense, around 190 meV. For D_3S, the peaks are shifted to lower frequencies, as expected due to the greater mass of deuterium atoms, with maxima centered around 90 meV and 130 meV, respectively. In both hydrides, the whole optical spectra from 30-40 meV to the Debye frequency contribute to the total electron-phonon coupling, which is found to be $\lambda = 2.3$ for H_3S and $\lambda = 2.2$ for D_3S, respectively. These values and the corresponding $\alpha^2F(\omega)$ functions are in excellent agreement with those reported in Refs. [49, 71, 72].

The solution of the AME equations reveals that H_3S and D_3S are single-gap superconductors with a broad energy gap distribution. Compared to the FSR treatment, the FBW calculation with fixed μ lowers the gap energy [see Figs. 2**(c)** and **(e)**]. This effect is even more pronounced when updating μ self-consistently (FBW+μ), as the chemical potential is shifted to higher energies, moving the Fermi level away from the peak of the van Hove singularity. These results emphasize the critical role of the VHS on the superconducting properties of H_3S, as has been pointed out in other works as well [48, 71, 73–75].

The highest measured T_c in the study of Drozdov et al. [50] is 203 K at 155 GPa for H_3S and 152 K at 173 GPa for D_3S,

with a variation of T_c for different samples of up to 15 K. Samples with better crystallinity for H_3S were later obtained by Mozaffari et al. [57] with a T_c of 201 K at 155 GPa and a small transition width of 5.5 K; and also by Nakao et al. [56], where a sharp drop of the resistance was measured at $T_c = $ 200 K at 150 GPa. Minkov et al. [59] have used the same direct in-situ synthesis from elemental S and excess H_2 as in Refs. [56, 57] to obtain better homogeneous samples for D_3S, revealing that D_3S reached a maximum T_c of 166 K at 157 GPa, significantly higher ($\approx 10\%$ difference) than previously reported values [50].

As can be appreciated in Tab. I, FBW+μ performs best in approaching the experimental critical temperatures T_c^{exp} among the different implementations for solving the AME equations. For H_3S, our calculations provide $T_c = 232$ K at 200 GPa, a percentage difference of 23-30% compared to the experimental values of 172-184 K at 200 GPa from Refs. [50, 53, 59]. The rather large differences originate from anharmonicity and the quantum motion of the nuclei, which are known to play a crucial role in H_3S [68]. Incorporating these effects is, in principle, possible within EPW, as demonstrated in Refs. [70, 76] for example, but beyond the scope of the current work. Here, it is important to point out that FBW+μ provides a much better estimate for T_c than FSR. The performance of FBW+μ in reproducing the experimental values is notably better for D_3S, where anharmonic and quantum ionic effects are smaller. The full-bandwidth treatment only

Table I. **Summary of the obtained superconducting properties for YH_6, CaH_6, H_3S, and D_3S:** The table lists the DOS $N(\varepsilon_F)$ and the H partial DOS $N_H(\varepsilon_F)$ at the Fermi level, the electron-phonon coupling parameter λ, the logarithmic average of the phonon frequencies ω_{log}, and the superconducting critical temperature T_c according to the modified McMillan formula (mMc), the University of Florida machine-learning model (UF), the Fermi-surface-restricted approximation (FSR), and the full-bandwidth implementation without (FBW) and with (FBW+μ) the self-consistent chemical potential update scheme, and all experimental critical temperatures T_c^{exp} at 200 GPa available in the literature. The T_c^{exp} of Ref. [21] and Ref. [26] are used as reference for YH_6 and CaH_6, respectively; and the T_c^{exp} of Refs. [50, 53, 59] are used as reference for H_3S and D_3S.

	$N(\varepsilon_F)$ [$N_H(\varepsilon_F)$] (eV^{-1})	λ	ω_{log} (meV)	T_c^{mMc} (K)	T_c^{UF} (K)	T_c^{FSR} (K)	T_c^{FBW} (K)	$T_c^{FBW+\mu}$ (K)	T_c^{exp} (K)
YH_6	0.69 [0.32]	2.0	108	154	202	250	239	238	208-214
CaH_6	0.31 [0.27]	2.0	104	148	188	205	200	198	$\sim$ 204
H_3S	0.53 [0.27]	2.3	108	173	232	256	250	232	172-184
D_3S	0.53 [0.27]	2.2	80	127	166	190	182	170	144-148

slightly modifies the structure of the superconducting gap Δ_{nk}, i.e., the gap distributions are shifted to lower energies while retaining the overall shape at each temperature.

The isotope effect coefficient, according to the BCS theory, is given by

$$\alpha = -\frac{\ln T_c^{D_3S} - \ln T_c^{H_3S}}{\ln M_D - \ln M_H}, \tag{1}$$

where M_H and M_D are the atomic mass of hydrogen and deuterium. The experimental values obtained for α are around 0.47 at 150 GPa [52]. Within FSR, we obtain $\alpha = 0.54$ at 200 GPa; for FBW we have $\alpha = 0.48$; and for FBW+μ we have $\alpha = 0.45$.

These results demonstrate that the full-bandwidth method is imperative for accurately describing these systems within the Eliashberg formalism. As already pointed out by other authors [48, 71, 73], the conventional Eliashberg formalism within the FSR framework partially fails to accurately describe the T_c behavior in H_3S due to a substantial variation of the DOS near ε_F originating from the van Hove-type singularity present there. The strong el-ph coupling of $\lambda = 2.3$ for H_3S and $\lambda = 2.2$ for D_3S, and the broad distribution of α^2F over the vibrational spectra makes this scenario even more dramatic since the region around ε_F, where the phonon scattering dominates over the Coulomb repulsion, is strongly enhanced by the el-ph interactions. Lastly, these results highlight the importance of updating the chemical potential while solving the AME equations within the FBW treatment.

At the end of this section, we also want to shortly discuss the modified McMillan [65, 66] formula and a recent machine-learning approach to improve upon it [67], both of which can be used as an almost instant way to predict T_c, but do not offer insight into other properties of the superconducting state. The modified McMillan formula (mMc, see Supplementary Note 1) is obtained from the Eliashberg theory by defining moments of the α^2F spectral function and fitting an equation to match the experimental T_c, taking into account a bit more than 200 data points. As the data set consisted of the (low-T_c) superconductors known at the time and a few pure model calculations, it does not reproduce the experimental critical temperatures of the extreme cases of contemporary

highly-compressed high-T_c materials, as is also evident for the materials chosen in this study [66].

The machine-learned equation proposed by a group of the University of Florida (UF), on the other hand, has been trained to match the solutions of the Migdal-Eliashberg equations with a dataset of thousands of real and artificially generated α^2F functions, including high-pressure, high-T_c hydrides as well. It thus performs much better than the mMc formula and matches the results obtained with AME fairly well. It is therefore a viable tool to determine an accurate value for T_c quickly but does not offer insight into the superconducting gap function and its energy distribution, the superconducting DOS, and so on. We also observe shortcomings when trying to simulate the effects of doping, as detailed in the next section.

Application to doped hydrides

Doping can be a powerful method to tailor and fine-tune specific material properties, especially in electronic applications. It has been used to metallize semiconducting phases, induce superconductivity, and optimize specific properties of the superconducting phase [41, 42, 77–80]. In particular, this approach has been employed to increase the T_c in known superconducting systems and is claimed to be a route to obtain (or to be the source of) room-temperature superconductivity in recently reported hydrides [64, 81–87].

The doping of hydrogen-rich superconductors and its tentatively beneficial effect on T_c has been extensively studied in various works [83, 84, 88–98], however, most of the theoretical predictions for an enhancement of T_c rely on calculations based on the McMillan/Allen-Dynes formulas, or on the ME equations within the constant-DOS approximation, and hence focus mainly on maximizing the value of the DOS at the Fermi level and thereby that of λ. In particular, in systems with VHS-like peaks close to the Fermi level, this approach might severely overestimate the contribution of the electronic states available for the superconducting pairing and thus also the critical temperature. Furthermore, the exact value of the DOS close to a VHS-like shape is subject to large variations, which makes predictions even more error-prone [73].
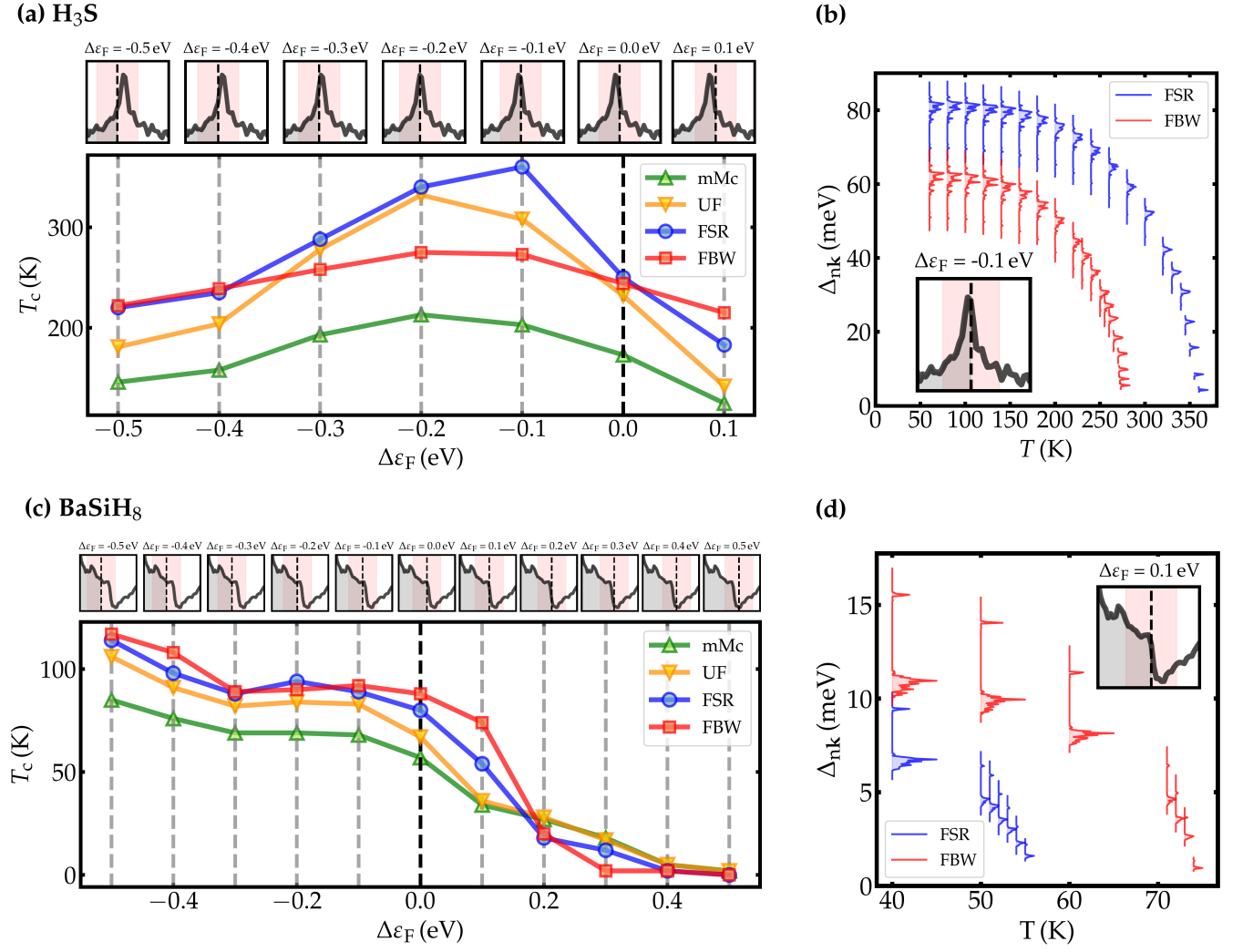
Figure 3. Doping effects on the critical temperature in different approaches: Effects of doping (shifting the Fermi level) in H_3S at 200 GPa (panels **(a)** and **(b)**) and $BaSiH_8$ at 30 GPa (panels **(c)** and **(d)**). Panel **(a)** shows the superconducting critical temperature T_c as a function of the Fermi level shift $\Delta\varepsilon_F$, obtained within the mMc formula (green), the UF equation (orange), the FSR approximation (blue), and the FBW approach (red). The smaller subpanels on top show the corresponding DOS in a range of ± 2 eV around the unshifted Fermi energy ε_F, where the dashed lines mark the position of $\varepsilon_F + \Delta\varepsilon_F$ and the shaded red areas highlight the included electronic energy range of $\varepsilon_F + \Delta\varepsilon_F \pm 1$ eV. Panel **(b)** displays the distribution of the values of the anisotropic superconducting gap Δ_{nk} on the Fermi surface within the FSR (blue) and FBW (red) approach for H_3S with $\Delta\varepsilon_F = -0.1$ eV, where we find the maximum absolute difference between the FSR and FBW T_c (see blue and red lines in **(a)**). The inset shows the corresponding DOS subpanel from **(a)**. Panels **(c)** and **(d)** show the corresponding results for $BaSiH_8$ at 30 GPa, where we find the maximum T_c difference for $\Delta\varepsilon_F = +0.1$ eV.

With the FBW implementation, we overcome these problems and limitations as demonstrated for H_3S and $BaSiH_8$, two materials exhibiting considerable variation in the DOS around the Fermi level. Applying doping via a rigid band shift, we explore the different regions of increased, maximal, and lowered DOS, and discuss the effects on T_c within the mMc and MD formulas, and the FSR and FBW methods. We want to note here that for these calculations we do not update the chemical potential, as an explicit shift in the Fermi level can also be interpreted as a shift in the chemical potential, and hence such a calculation can be reproduced by one with a (slightly) different effective shift.

H_3S

The well-studied hydride superconductor H_3S is a perfect candidate material where doping to optimize T_c appears very tempting due to the VHS-like peak in the DOS in close proximity to the Fermi level, as shown in Fig. 3**(a)**-**(b)**. Many theoretical works have considered doping of H_3S to increase its T_c estimates, choosing dopants to bring the system's Fermi level closer to the maximum of the VHS-like peak. The stability of the $Im\bar{3}m$ H_3S structure with incorporation of various elements has been systematically investigated using either the direct supercell approach with substitutional dop-

ing or the virtual crystal approximation, followed by T_c estimates based on the mMc formula or the isotropic FSR approach [83, 88–93, 95, 98–100].

While adding dopants may increase the T_c by also enhancing the el-ph coupling, we want to specifically address the effect of a change in the number of available electronic states. To this end, we solved the AME equations in the FSR and FBW frameworks for shifts of the Fermi level $\Delta\varepsilon_F$ between -0.5 eV and 0.1 eV in steps of 0.1 eV, corresponding to changes in the electron number Δ_{elec} of -0.30, -0.26, -0.20, -0.13, -0.06, and +0.05.

In Fig. 3(**a**), we present the T_c values obtained within the FSR and FBW treatments of the AME equations and the results obtained using the mMc and UF semi-empirical formulas mentioned earlier. The T_c values are plotted as a function of $\Delta\varepsilon_F$ demonstrating that all approaches show a clear correlation between T_c and DOS with the maximum T_c occurring at around $\Delta\varepsilon_F \sim -0.1$ eV to -0.2 eV, as highlighted in Fig. 3(**b**).

However, within the FSR approximation, there is a notable and unphysical increase in T_c values around the maximum of the DOS. This behavior can be attributed to the limitation of the constant-DOS assumption in the FSR approach. Similarly, the UF model exhibits a strong dependence on doping. In contrast, the AME solutions in the FBW approach, which consider the full energy dependence of the DOS, exhibit a much less pronounced effect of doping on T_c. Finally, the semi-empirical mMc formula consistently underestimates T_c for strongly coupled systems when compared to results obtained from the AME equations.

In the context of our analysis of a doped H_3S system, we would like to address the topic of speculated room temperature superconductivity within this system [101]. Considering that the experimental T_c values for pure H_3S are around or below 200 K, and that the FBW calculations only show a maximum increase in T_c of about 5-10% upon doping (see Fig. 4), achieving a conventional superconducting state at room temperature in the H_3S parent phase remains elusive; at least within the assumption that the slight doping leaves the electronic structure unaltered.

On a more technical note, we want to add that VHS-like features also pose other problems when trying to arrive at robust numerical results. For example, the exact value of the DOS at the VHS-like peak is difficult to converge and requires extremely dense **k**-grids and small smearing values. To demonstrate this, we examined the VHS region by performing additional calculations with two different smearing values σ for the energy-conserving δ-functions. The results are shown in Figure 4. The critical temperature obtained with the FSR approximation is very sensitive to the smearing value chosen, the largest deviation in T_c reaching up to 70 K, whereas the FBW implementation is considerably more robust, with at most a 10 K difference between the different smearing values tested. The reason for that is that the only quantity impacted by smearing in the FBW implementation is the screened Coulomb interaction term in Eq. (15), whereas smearing impacts all FSR equations via $N(\varepsilon_F)$ and
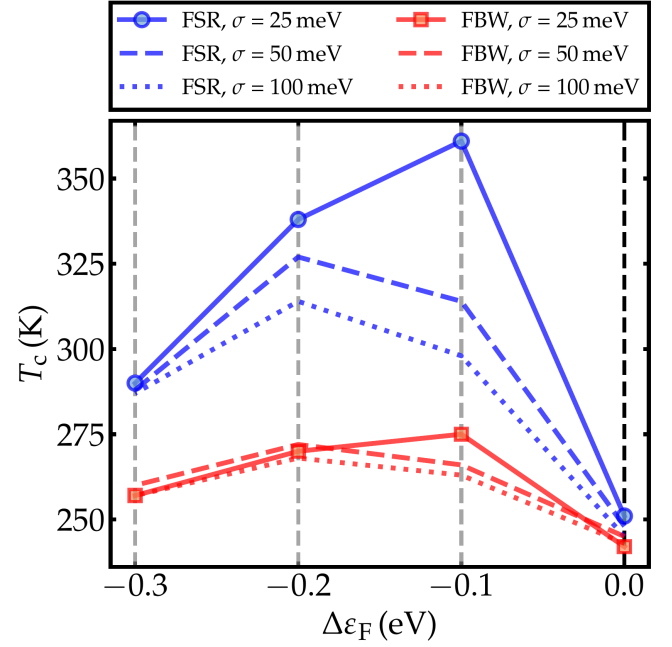

Figure 4. **Dependence of the doped T_c results on the electronic smearing:** Influence of the smearing value σ for the energy-conserving δ-functions on the T_c of doped H_3S within the FSR (blue) and FBW (red) approach as a function of the Fermi energy shift $\Delta\varepsilon_F$. The solid lines represent the corresponding results shown in Figure 3(**a**) for a smearing value of $\sigma = 25$ meV, the dashed (dotted) lines represent the results for $\sigma = 50$ (100) meV.

$\delta(\varepsilon_{m\mathbf{k+q}} - \varepsilon_F)$ (see Eqs. 18 and 19). As a result, besides being more rigorous, the FBW implementation also considerably improves convergence behavior for materials exhibiting a strongly varying DOS.

$BaSiH_8$

The $Fm\bar{3}m$ phase of $BaSiH_8$ was recently predicted and described in detail by some of the current authors [37, 70]. This ternary hydride has the crystal structure of the XYH_8 template first introduced for $LaBH_8$ [63], also assumed by other high-T_c superhydrides that are stable at moderate pressures [27, 102], like the recently synthesized LaBe-compound [28]. Up to now, $BaSiH_8$ is the XYH_8 compound with the lowest predicted pressure of dynamical stability of 5 GPa within the harmonic phonon theory. A more realistic estimate for the critical pressure of stability and synthesizability is provided by considering the kinetic stability of the compound, which places stability at a pressure above 30 GPa [37, 70].

Independent of the actual critical pressure, this material exhibits a step-like feature around the Fermi level, with an almost constant region of high DOS below the Fermi level and a sharp drop to a region of very low DOS above ε_F, as can be

appreciated in Fig. 3(**c**), making it another perfect test bed to compare the FSR and FBW approaches.

We solved the AME equations within FSR and FBW approaches for shifts of the Fermi level $\Delta\varepsilon_F$ between $-0.5\,\text{eV}$ and $0.5\,\text{eV}$ in steps of $0.1\,\text{eV}$, corresponding to changes in the electron number Δ_{elec} of -0.52, -0.42, -0.31, -0.21, -0.10, +0.09, +0.15, +0.18, +0.20, and +0.22. In Figs. 3(**c**) and (**d**), we show the T_c values obtained for the two levels of approximations as a function of $\Delta\varepsilon_F$. As before, T_c roughly follows the shape of the DOS, but, in contrast to H_3S, we observe a considerable increase in T_c for $BaSiH_8$ when employing the more rigorous FBW approach. Already in the undoped case the T_c is raised to $87\,\text{K}$, which can be further increased by doping to about $92\,\text{K}$ when shifting the Fermi level by $-0.1\,\text{eV}$. This would place the critical superconducting temperature of $BaSiH_8$ above the technologically extremely important threshold set by the boiling temperature of nitrogen.

The behaviour of T_c with respect to Fermi level shifts for the different methods is quite complex: For a shift of $-0.1\,\text{eV}$ or below the AME results are similar and also agree with the UF model, while mMc gives considerably lower values for T_c. In a region around $0.1\,\text{eV}$ shift, the FBW implementation predicts a larger value for T_c than FSR, and the simple mMc and UF formulas provide an even smaller estimate. For ε_F-shifts larger than $0.2\,\text{eV}$, mMc and UF actually give the largest values for T_c and FBW the smallest. In other words, while the dependence of T_c with respect to Fermi level shifts was smallest in FBW for H_3S, it is actually varying the strongest within FBW for $BaSiH_8$.

These intricate results underscore the importance of taking into account the energy dependence of the electronic DOS around the Fermi level, in particular for systems where the DOS is either strongly peaked close to ε_F [84, 86, 103–105], as for H_3S, or highly asymmetric [76, 106–109], as for $BaSiH_8$. In that light, we believe that the agreement between experimental measurements and theoretical predictions can be considerably improved by employing the FBW method not only for the class of superhydrides but also for other material systems showing similar features in the DOS [42, 45, 110–118].

DISCUSSION

In summary, we have employed the anisotropic Migdal-Eliashberg formalism within the full-bandwidth formulation utilizing maximally-localized Wannier functions as implemented in the EPW suite. This approach enables us to calculate the momentum- and band-resolved superconducting gap more accurately, taking into account the electron-phonon scattering processes around the Fermi level, and not only restricted to the Fermi surface. In addition, we introduced a sparse, non-uniform sampling scheme over the imaginary Matsubara frequencies, which shows similar accuracy and much-improved efficiency compared to the uniform sampling scheme.

To validate the robustness of our methodology, we conducted comprehensive tests on two representative classes of superhydrides: the sodalite-like clathrates YH_6 and CaH_6, as well as the covalent hydrides H_3S and D_3S. To assess the accuracy of our approach, we compared our results with previous ab-initio calculations and experimental data. Our results unequivocally demonstrate the indispensable role of the full-bandwidth formulation, particularly for compounds characterized by narrow bands or critical points in proximity to the Fermi level. A noteworthy illustration of the importance of employing the FBW formulation is evident in the case of H_3S, which possesses a van Hove singularity. Our methodology effectively captures the intricate behavior of such systems, highlighting the superiority of the FBW approach in these critical scenarios. Furthermore, we emphasize the crucial impact of the chemical potential updating scheme within the FBW formulation, which substantially contributes to accurately describing the superconducting phase in these challenging cases. This aspect proves to be a vital component in achieving a comprehensive understanding of the superconducting properties of these complex materials.

In addition, we applied the FBW approach to investigate electron- and hole-doped hydride superconductors, namely H_3S and the recently predicted low-pressure $BaSiH_8$. These materials serve as prime examples of systems with distinct DOS features that deviate significantly from the constant-DOS assumption made in the FSR approximation. Previous studies have often focused on maximizing the DOS specifically at the Fermi level, aiming to design high(er)-T_c superconductors by doping the system to shift ε_F to the maximum of a VHS-like structure. Our calculations reveal significant pitfalls associated with such a simplistic FSR-based approach. We find instances of pronounced under- or overestimation of T_c, highlighting the critical importance of adopting the FBW method, particularly in scenarios with strongly peaked DOS or closely adjacent DOS regions exhibiting extremely high and low values. By employing the FBW approach, we can accurately capture the intricate interplay of DOS features and better predict the behavior of superconductors in these complex cases. This sheds light on the limitations of the FSR approach and underscores the significance of our advanced methodology in studying and engineering novel superconducting materials with tailored properties for real-world applications.

METHODS

Anisotropic Migdal-Eliashberg theory

The Eliashberg theory is a powerful many-body perturbation approach for describing conventional superconductors, where the Cooper pairing between two electrons stems from the interplay between the attractive el-ph coupling and the repulsive screened Coulomb interaction [8, 119]. The Nambu-Gor'kov's formalism [120, 121] with a generalized matrix

Green's function can be used to formulate the Eliashberg theory. The on- and off-diagonal elements of the 2×2 Green's function matrix describe the single-particle excitations in the normal state and Cooper-pair amplitudes in the superconducting state, corresponding to the standard and anomalous Green's functions, respectively [11, 32, 120–124]. The transition from normal to superconducting state manifests in anomalous Green's functions becoming nonzero below a material specific critical temperature.

The matrix Green's function is obtained from the Dyson equation

$$\hat{G}_{n\mathbf{k}}^{-1}(i\omega_j) = \left[\hat{G}_{n\mathbf{k}}^0(i\omega_j)\right]^{-1} - \hat{\Sigma}_{n\mathbf{k}}^{\text{pa}}(i\omega_j), \tag{2}$$

where $\hat{G}_{n\mathbf{k}}^0(i\omega_j)$ is the non-interacting Green's function in the normal state with band index n and wavevector $\mathbf{k}$, $\hat{\Sigma}_{n\mathbf{k}}^{\text{pa}}(i\omega_j)$ is the pairing self-energy, and $i\omega_j = i(2j + 1)\pi T$ is the fermionic Matsubara frequency with T being the absolute temperature and j an integer. An expression for the self-energy in terms of the electron Green's function can be obtained with the el-ph and electron-electron contributions given by the Migdal [7, 123] and GW [125, 126] approximations, respectively:

$$\hat{\Sigma}_{n\mathbf{k}}^{\text{pa}}(i\omega_j) = \hat{\Sigma}_{n\mathbf{k}}^{\text{ep}}(i\omega_j) + \hat{\Sigma}_{n\mathbf{k}}^{\text{c}}(i\omega_j). \tag{3}$$

Using the Pauli matrices, $\hat{\tau}_0 = \left(\begin{smallmatrix} 1 & 0 \\ 0 & 1 \end{smallmatrix}\right), \hat{\tau}_1 = \left(\begin{smallmatrix} 0 & 1 \\ 1 & 0 \end{smallmatrix}\right), \hat{\tau}_2 = \left(\begin{smallmatrix} 0 & -i \\ i & 0 \end{smallmatrix}\right), \hat{\tau}_3 = \left(\begin{smallmatrix} 1 & 0 \\ 0 & -1 \end{smallmatrix}\right)$, the el-ph and Coulomb contributions to the self-energy can be expressed as

$$\hat{\Sigma}_{n\mathbf{k}}^{\text{ep}}(i\omega_j) = -T \sum_{mj'\nu} \int \frac{d\mathbf{q}}{\Omega_{\text{BZ}}} \hat{\tau}_3 \hat{G}_{m\mathbf{k}+\mathbf{q}}(i\omega_{j'})\hat{\tau}_3$$
$$\times |g_{mn\nu}(\mathbf{k}, \mathbf{q})|^2 D_{\mathbf{q}\nu}(i\omega_j - i\omega_{j'}), \tag{4}$$

and

$$\hat{\Sigma}_{n\mathbf{k}}^{\text{c}}(i\omega_j) = -T \sum_{mj'} \int \frac{d\mathbf{q}}{\Omega_{\text{BZ}}} \hat{\tau}_3 \hat{G}_{m\mathbf{k}+\mathbf{q}}^{\text{od}}(i\omega_{j'})\hat{\tau}_3 V_{n\mathbf{k},m\mathbf{k}+\mathbf{q}}, \tag{5}$$

where Ω_{BZ} is the BZ volume, $D_{\mathbf{q}\nu}(i\omega_l) = 2\omega_{\mathbf{q}\nu}/[(i\omega_l)^2 - \omega_{\mathbf{q}\nu}^2]$ is the dressed phonon propagator for phonons with wavevector $\mathbf{q}$ and branch index ν, $i\omega_l = i2l\pi T$ is the bosonic Matsubara frequency with l an integer, $g_{mn\nu}(\mathbf{k}, \mathbf{q})$ is the screened el-ph matrix element for the scattering between the electronic states $n\mathbf{k}$ and $m\mathbf{k} + \mathbf{q}$ through a phonon of frequency $\omega_{\mathbf{q}\nu}$, and $V_{n\mathbf{k},m\mathbf{k}+\mathbf{q}}$ is the static screened Coulomb interaction between electrons [123, 127]. In Eq. (5), only the off-diagonal components of the Green's function $\hat{G}_{n\mathbf{k}}^{\text{od}}(i\omega_j)$ are retained in order to avoid double counting the Coulomb effects that are already included in $\hat{G}_{n\mathbf{k}}^0(i\omega_j)$ [123].

The anisotropic el-ph coupling strength is described as

$$\lambda_{n\mathbf{k},m\mathbf{k}+\mathbf{q}}(\omega_j - \omega_{j'}) = N(\varepsilon_{\text{F}}) \sum_{\nu} \frac{2\omega_{\mathbf{q}\nu} |g_{mn\nu}(\mathbf{k}, \mathbf{q})|^2}{(\omega_j - \omega_{j'})^2 + \omega_{\mathbf{q}\nu}^2}, \tag{6}$$

with $N(\varepsilon_{\text{F}})$ the DOS per spin at the Fermi level. Eq. (6) can be used to rewrite the el-ph self-energy in Eq. (4), which can

then be taken together with Eq. (5) and inserted into Eq. (3). The pairing self-energy then becomes:

$$\hat{\Sigma}_{n\mathbf{k}}^{\text{pa}}(i\omega_j) = \frac{T}{N(\varepsilon_{\text{F}})} \sum_{mj'} \int \frac{d\mathbf{q}}{\Omega_{\text{BZ}}}$$
$$\times \left\{\lambda_{n\mathbf{k},m\mathbf{k}+\mathbf{q}}(\omega_j - \omega_{j'})\hat{\tau}_3 \hat{G}_{m\mathbf{k}+\mathbf{q}}(i\omega_{j'})\hat{\tau}_3\right.$$
$$\left. - N(\varepsilon_{\text{F}})V_{n\mathbf{k},m\mathbf{k}+\mathbf{q}}\hat{\tau}_3 \hat{G}_{m\mathbf{k}+\mathbf{q}}^{\text{od}}(i\omega_{j'})\hat{\tau}_3\right\} \tag{7}$$

To replace $\hat{G}_{n\mathbf{k}}(i\omega_j)$ in Eq. (7), we expand the two components of the Dyson equation (2) in terms of the Pauli matrices as

$$\left[\hat{G}_{n\mathbf{k}}^0(i\omega_j)\right]^{-1} = i\omega_j\hat{\tau}_0 - (\varepsilon_{n\mathbf{k}} - \mu)\hat{\tau}_3, \tag{8}$$

where $\varepsilon_{n\mathbf{k}}$ are the Kohn-Sham eigenenergies, and

$$\hat{\Sigma}_{n\mathbf{k}}^{\text{pa}}(i\omega_j) = i\omega_j\left[1 - Z_{n\mathbf{k}}(i\omega_j)\right]\hat{\tau}_0 + \chi_{n\mathbf{k}}(i\omega_j)\hat{\tau}_3$$
$$+ \phi_{n\mathbf{k}}(i\omega_j)\hat{\tau}_1 + \bar{\phi}_{n\mathbf{k}}(i\omega_j)\hat{\tau}_2. \tag{9}$$

In Eq. (9), we introduced the mass renormalization function $Z_{n\mathbf{k}}(i\omega_j)$, the energy shift $\chi_{n\mathbf{k}}(i\omega_j)$, and the order parameter $\phi_{n\mathbf{k}}(i\omega_j)$. Inserting Eqs. (8) and (9) into Eq. (2), and inverting the resulting matrix leads to the following expression for $\hat{G}_{n\mathbf{k}}(i\omega_j)$:

$$\hat{G}_{n\mathbf{k}}(i\omega_j) = \frac{1}{\det[\hat{G}_{n\mathbf{k}}^{-1}(i\omega_j)]}\left\{i\omega_j Z_{n\mathbf{k}}(i\omega_j)\hat{\tau}_0\right.$$
$$\left. +\left[\varepsilon_{n\mathbf{k}} - \mu + \chi_{n\mathbf{k}}(i\omega_j)\right]\hat{\tau}_3 + \phi_{n\mathbf{k}}(i\omega_j)\hat{\tau}_1 + \bar{\phi}_{n\mathbf{k}}(i\omega_j)\hat{\tau}_2\right\} \tag{10}$$

It can be easily verified that $\phi_{n\mathbf{k}}(i\omega_j)$ and $\bar{\phi}_{n\mathbf{k}}(i\omega_j)$ are proportional within an arbitrary phase, and without loss of generality, one can choose the relative phase such that $\bar{\phi}_{n\mathbf{k}}(i\omega_j) = 0$ [30, 123]. Eq. (10) with $\bar{\phi}_{n\mathbf{k}}(i\omega_j) = 0$ can be used to rewrite Eq. (7) for the pairing self-energy as:

$$\hat{\Sigma}_{n\mathbf{k}}^{\text{pa}}(i\omega_j) = -\frac{T}{N(\varepsilon_{\text{F}})} \sum_{mj'} \int \frac{d\mathbf{q}}{\Omega_{\text{BZ}}} \frac{1}{\theta_{m\mathbf{k}+\mathbf{q}}(i\omega_{j'})}$$
$$\times \left\{i\omega_{j'} Z_{m\mathbf{k}+\mathbf{q}}(i\omega_{j'})\lambda_{n\mathbf{k},m\mathbf{k}+\mathbf{q}}(\omega_j - \omega_{j'})\hat{\tau}_0\right.$$
$$+\left[\varepsilon_{m\mathbf{k}+\mathbf{q}} - \mu + \chi_{m\mathbf{k}+\mathbf{q}}(i\omega_{j'})\right]\lambda_{n\mathbf{k},m\mathbf{k}+\mathbf{q}}(\omega_j - \omega_{j'})\hat{\tau}_3$$
$$\left. -\phi_{m\mathbf{k}+\mathbf{q}}(i\omega_{j'})\left[\lambda_{n\mathbf{k},m\mathbf{k}+\mathbf{q}}(\omega_j - \omega_{j'}) - N(\varepsilon_{\text{F}})V_{n\mathbf{k},m\mathbf{k}+\mathbf{q}}\right]\hat{\tau}_1\right\}, \tag{11}$$

where

$$\theta_{n\mathbf{k}}(i\omega_j) = -\det[\hat{G}_{n\mathbf{k}}^{-1}(i\omega_j)]|_{\bar{\phi}_{n\mathbf{k}}(i\omega_j)=0}$$
$$= \left[\omega_j Z_{n\mathbf{k}}(i\omega_j)\right]^2 + \left[\varepsilon_{n\mathbf{k}} - \mu + \chi_{n\mathbf{k}}(i\omega_j)\right]^2$$
$$+ \left[\phi_{n\mathbf{k}}(i\omega_j)\right]^2. \tag{12}$$

Equating the different components of the Pauli matrix elements in Eqs. (9) and (11) leads to a system of three coupled non-linear equations:

$$Z_{n\mathbf{k}}(i\omega_j) = 1 + \frac{T}{\omega_j N(\varepsilon_F)} \sum_{mj'} \int \frac{d\mathbf{q}}{\Omega_{BZ}} \frac{\omega_{j'} Z_{m\mathbf{k}+\mathbf{q}}(i\omega_{j'})}{\theta_{m\mathbf{k}+\mathbf{q}}(i\omega_{j'})}$$
$$\times \lambda_{n\mathbf{k},m\mathbf{k}+\mathbf{q}}(\omega_j - \omega_{j'})$$
(13)

$$\chi_{n\mathbf{k}}(i\omega_j) = -\frac{T}{N(\varepsilon_F)} \sum_{mj'} \int \frac{d\mathbf{q}}{\Omega_{BZ}} \frac{\varepsilon_{m\mathbf{k}+\mathbf{q}} - \mu + \chi_{m\mathbf{k}+\mathbf{q}}(i\omega_{j'})}{\theta_{m\mathbf{k}+\mathbf{q}}(i\omega_{j'})}$$
$$\times \lambda_{n\mathbf{k},m\mathbf{k}+\mathbf{q}}(\omega_j - \omega_{j'})$$
(14)

$$\phi_{n\mathbf{k}}(i\omega_j) = \frac{T}{N(\varepsilon_F)} \sum_{mj'} \int \frac{d\mathbf{q}}{\Omega_{BZ}} \frac{\phi_{m\mathbf{k}+\mathbf{q}}(i\omega_{j'})}{\theta_{m\mathbf{k}+\mathbf{q}}(i\omega_{j'})}$$
$$\times \left[\lambda_{n\mathbf{k},m\mathbf{k}+\mathbf{q}}(\omega_j - \omega_{j'}) - N(\varepsilon_F) V_{n\mathbf{k},m\mathbf{k}+\mathbf{q}} \right]$$
(15)

This set of equations is supplemented with an equation for the electron number, which determines the chemical potential μ [127, 128]:

$$N_e = \sum_n \int \frac{d\mathbf{k}}{\Omega_{BZ}} \left[1 - 2T \sum_j \frac{\varepsilon_{n\mathbf{k}} - \mu + \chi_{n\mathbf{k}}(i\omega_j)}{\theta_{n\mathbf{k}}(i\omega_j)} \right], \quad (16)$$

where N_e is the number of electrons per unit cell (see Supplementary Method 1 for a discussion about the electron number equation).

Equations (13)-(16) involve electronic states that are not restricted to the Fermi surface or its immediate vicinity; hence, labeled as anisotropic full-bandwidth (FBW) Migdal-Eliashberg equations [129]. We have recently implemented the above-described anisotropic FBW approach in the EPW code [31].

The set of coupled equations can be solved self-consistently at various temperatures for the temperature-dependent superconducting gap $\Delta_{n\mathbf{k}}$, given by:

$$\Delta_{n\mathbf{k}}(i\omega_j) = \frac{\phi_{n\mathbf{k}}(i\omega_j)}{Z_{n\mathbf{k}}(i\omega_j)}. \quad (17)$$

The Padé approximation [130, 131] can then be used to obtain the continuation of $\Delta_{n\mathbf{k}}(i\omega_j)$ from the imaginary to the real axis. The superconducting temperature T_c is the highest temperature at which $\phi_{n\mathbf{k}}(i\omega_j) \neq 0$ has a nontrivial solution.

The contribution of the Coulomb interaction to the Eliashberg equation, through matrix elements $V_{n\mathbf{k},m\mathbf{k}+\mathbf{q}}$, can be evaluated at the same level as the el-ph interaction for the simpler versions of the Eliashberg formalism [48, 69, 72, 132, 133]. To reduce the computational cost, however, the common approach is to replace the $N(\varepsilon_F) V_{n\mathbf{k},m\mathbf{k}+\mathbf{q}}$ terms with the semi-empirical Morel-Anderson pseudopotential μ^* [134]. In practice, the numerical value of this parameter is connected with

the cutoff frequency ω_{max} of the Matsubara frequencies. With a typical choice of ω_{max} being ten times the maximum phonon frequency ω_{ph}, a value of $\mu^* = 0.1$–0.2 results in a satisfactory agreement with experiment for many applications. The μ^* can also be calculated from first-principles, using the double Fermi surface average of $V_{n\mathbf{k},m\mathbf{k}+\mathbf{q}}$ [12, 43, 60, 63].

The numerical solution of the anisotropic FBW Migdal-Eliashberg equations is computationally very demanding. A common simplification of these equations consists in restricting the energy range close to the Fermi level by introducing the unity factor $\int_{-\infty}^{+\infty} d\varepsilon \, \delta(\varepsilon_{n\mathbf{k}} - \varepsilon)$, and to assume that the DOS within this energy window is constant [11, 32, 123, 127, 135–138]. It can be shown that, within these approximations, the energy shift $\chi_{n\mathbf{k}}$ vanishes and the requirement in Eq. ((16)) is automatically satisfied. As a result, only two equations for $Z_{n\mathbf{k}}(i\omega_j)$ and $\phi_{n\mathbf{k}}(i\omega_j)$ need to be solved self-consistently:

$$Z_{n\mathbf{k}}(i\omega_j) = 1 + \frac{\pi T}{N(\varepsilon_F)\omega_j} \sum_{mj'} \int \frac{d\mathbf{q}}{\Omega_{BZ}} \frac{\omega_{j'}}{\sqrt{\omega_{j'}^2 + \Delta_{m\mathbf{k}+\mathbf{q}}^2(i\omega_{j'})}}$$
$$\times \lambda_{n\mathbf{k},m\mathbf{k}+\mathbf{q}}(\omega_j - \omega_{j'}) \delta(\varepsilon_{m\mathbf{k}+\mathbf{q}} - \varepsilon_F) \quad (18)$$

$$Z_{n\mathbf{k}}(i\omega_j)\Delta_{n\mathbf{k}}(i\omega_j) = \frac{\pi T}{N(\varepsilon_F)} \sum_{mj'} \int \frac{d\mathbf{q}}{\Omega_{BZ}} \frac{\Delta_{m\mathbf{k}+\mathbf{q}}(i\omega_{j'})}{\sqrt{\omega_{j'}^2 + \Delta_{m\mathbf{k}+\mathbf{q}}^2(i\omega_{j'})}}$$
$$\times \left[\lambda_{n\mathbf{k},m\mathbf{k}+\mathbf{q}}(\omega_j - \omega_{j'}) - N(\varepsilon_F) V_{n\mathbf{k},m\mathbf{k}+\mathbf{q}} \right] \delta(\varepsilon_{m\mathbf{k}+\mathbf{q}} - \varepsilon_F)$$
(19)

Equations (18) and (19) are the anisotropic FSR Migdal-Eliashberg equations. They have been the basis for the superconductivity calculations in the EPW code prior to the recent developments [30, 32].

Sparse sampling of Matsubara frequencies

All calculated quantities in the Migdal-Eliashberg equations depend on Matsubara frequencies, which are proportional to the absolute temperature. This results in a computational challenge since solving these equations at low temperatures (e.g., necessary for low-T_c superconductors) requires a larger number of frequencies within the same energy range. As discussed in the previous section, for the FBW+μ method, one needs a Matsubara frequency cutoff 6-12 times the Fermi energy window in order to converge the chemical potential and, consequently, the superconducting gap energy, leading to a considerable increase in computational cost. While a frequency cutoff of 4 eV has been found to be sufficient for calculations with FSR and FBW with fixed chemical potential at the Fermi level in the case of H_3S, adopting FBW+μ required a Matsubara frequency 2-3 times larger as shown in Supplementary Figure 1.

The computational cost can be reduced by pruning the Matsubara frequencies [132]. We implemented a sparse sampling scheme, described in the following, in the EPW code as an

alternative to uniform sampling over the Matsubara frequencies. Denoting with integer N_j the numerical index for the jth Matsubara frequency, $i\omega_j = i(2N_j + 1)\pi T$, the uniform and sparse grids can be obtained as:

$$N_j = j; \quad j = 0, \pm 1, \pm 2, \pm 3, \cdots \quad (20)$$

and

$$N_j = N_{j-1} + \text{INT}\left[\exp\left(\frac{j}{N_{\max}W}\right)\right]$$
$$N_0 = 0 \text{ and } j = 1, 2, 3, \cdots \quad (21)$$

where INT[ ] is the rounding to the closest integer, W is an adjustable weight factor, and $N_{\max}$ is the maximum Matsubara index for a given energy cutoff $\omega_{\max}$ and temperature T:

$$N_{\max} = \text{INT}\left[\frac{1}{2}\left(\frac{\omega_{\max}}{\pi T} - 1\right)\right] \quad (22)$$

Eq. ((21)) can be used to generate a Matsubara frequency grid with indices $N_j \leq N_{\max}$. For negative indices, the corresponding frequency can be easily obtained as $\omega_{-(j+1)} = -\omega_j$ (with $j > 0$). The resulting mesh is uniform at lower frequencies, contributing the most to the summation in the Migdal-Eliashberg equations, and becomes logarithmically sparser with increasing the Matsubara frequency index.

Increasing (decreasing) W results in a denser (sparser) grid sampling. With the default setting of $W = 1.0$, the sparse sampling scheme produces approximately 30% fewer Matsubara frequencies than the uniform one, while the first $\sim$40% points of the grid are still uniformly distributed. Numerical tests show that this approach maintains the accuracy of more expensive calculations that use the full uniform grid.

We systematically evaluated this sampling approach by computing the superconducting gap function within the FBW+μ method using both the uniform and sparse sampling scheme over Matsubara frequencies up to 6 eV for H_3S, D_3S, YH_6, and CaH_6. The primary outcomes are presented in Supplementary Figure 2, where the temperature-dependent behavior of $\Delta_{n\mathbf{k}}$ is plotted for FBW+μ (blue lines) and FBW+μ+sparse (red lines). The results indicate that the sparse sampling method can accurately reproduce the superconducting gap structure obtained using the uniform sampling scheme. In summary, no significant difference was observed across all the compounds analyzed. Among all the hydrides, the largest deviation was observed for D_3S, with a difference of only 3 K compared to the uniform sampling, corresponding to a percentage difference of 1.8 %. For all other hydrides, the difference between the sparse and uniform schemes was only 1 K. Thus, the sparse sampling can quantitatively reproduce the results obtained with the uniform sampling, but with a computational cost of approximately 40 % lower.

Computational details

The electronic structure calculations are performed within the Kohn-Sham scheme [139] of the density functional theory [140] as implemented in the Quantum ESPRESSO suite [141–143]. The exchange and correlation effects are treated within the Perdew-Burke-Ernzerhof parametrization [144] using scalar-relativistic optimized norm-conserving Vanderbilt pseudopotentials [145, 146]. The Kohn-Sham orbitals are expanded in a plane-wave basis set with a kinetic-energy cutoff of 100 Ry for H_3S, D_3S, and CaH_6, and 80 Ry for YH_6 and $BaSiH_8$. The charge density is computed using Γ-centered Monkhorst-Pack $\mathbf{k}$-meshes [147] of 24^3 $\mathbf{k}$-points for H_3S, D_3S, and CaH_6, 16^3 $\mathbf{k}$-points for YH_6, and 12^3 $\mathbf{k}$-points for $BaSiH_8$. The Brillouin-zone integration employs a Methfessel-Paxton smearing [148] of 0.01 Ry for H_3S, D_3S, and $BaSiH_8$, and 0.04 Ry for YH_6 and CaH_6. All lattice parameters and internal degrees of freedom were fully relaxed to reach a ground-state convergence of 10^{-7} Ry in the total energy and 10^{-6} Ry/a_0 for forces acting on the nuclei. $BaSiH_8$ is relaxed to a pressure of 30 GPa, all other compounds to 200 GPa.

The dynamical matrices and the linear variation of the self-consistent potential are calculated within the density-functional perturbation theory [149] on a regular phonon grid of 4^3 $\mathbf{q}$-points for H_3S, D_3S, and 6^3 $\mathbf{q}$-points for YH_6, CaH_6, and $BaSiH_8$. The threshold for self-consistency is set to 10^{-14} or lower.

The maximally localized Wannier functions (MLWFs) are constructed using the Wannier90 code [33, 150]. In the case of H_3S and D_3S, 10 Wannier functions are used to describe the electronic states near the Fermi level. The Wannier orbitals are three H-s-like functions and seven functions with s, p, d_{xy}, d_{xz}, and d_{yz} angular momentum states associated with the S site, with a spatial spread ranging from $0.77\,\text{Å}^2$ to $1.53\,\text{Å}^2$. For YH_6, six H-s-like projections and five Y-d-like functions are used to construct the initial guess, resulting in a spatial spread between $1.74\,\text{Å}^2$ and $1.86\,\text{Å}^2$. For CaH_6, besides the six H-s-like projections, we also use sp and sp^3 hybrid orbital functions associated with the Ca site to construct the initial guess, yielding a spatial spread between $0.80\,\text{Å}^2$ and $1.20\,\text{Å}^2$. For $BaSiH_8$, we use H s, Si s, p, d_{z^2}, $d_{x^2-y^2}$, and Ba p, d orbitals, giving a total of 22 Wannier functions, resulting in spatial spreads between $1.04\,\text{Å}^2$ and $1.79\,\text{Å}^2$.

The fully anisotropic Migdal-Eliashberg equations [32] are solved using the EPW code [30, 31]. Electron energies, phonon frequencies, and electron-phonon matrix elements are computed on fine grids containing 48^3 $\mathbf{k}$- and $\mathbf{q}$-points for H_3S, D_3S, YH_6, and CaH_6, and 30^3 $\mathbf{k}$- and $\mathbf{q}$-points for $BaSiH_8$. The lower boundary for the phonon frequency is set to $5\,\text{cm}^{-1}$ for H_3S and D_3S, and $15\,\text{cm}^{-1}$ for YH_6, CaH_6, and $BaSiH_8$. The width of the Fermi window is set to 2 eV for H_3S, D_3S, YH_6, CaH_6, and $BaSiH_8$. We set the Matsubara frequency cutoff to $\omega_{\max} = 6$ eV. The smearing values for the energy-conserving δ-function and for the sum over $\mathbf{q}$-space in the el-ph coupling are set to 25 meV and 0.05 meV, respectively, for H_3S and D_3S, 150 meV and 0.15 meV for YH_6 and CaH_6, and 100 meV and 0.1 meV for $BaSiH_8$. We solved the equations adopting a Coulomb pseudopotential of $\mu^* = 0.16$

for all materials except BaSiH$_8$, where a value of 0.1 was chosen to be consistent with our previous works [37, 70]. The continuation of the superconducting gap along the imaginary axis to the real energy axis is determined by applying the approximate analytic continuation using Padé functions [130, 131].

The doping calculations within rigid band model are performed by shifting the Fermi level in EPW before interpolating the el-ph matrix elements. All anisotropic Migdal-Eliashberg calculations are performed for electronic energies of $\pm 1\,\mathrm{eV}$ around the (shifted) Fermi level and a Matsubara cutoff of $\omega_{\mathrm{max}} = 4\,\mathrm{eV}$, if not stated otherwise.

DATA AVAILABILITY

CODE AVAILABILITY

ACKNOWLEDGEMENTS

AUTHOR CONTRIBUTIONS

RL and PPF contributed equally. RL and PPF performed the EPW calculations, prepared the figures and tables, and wrote the main draft. SH implemented the FBW formulation and the sparse sampling scheme in the superconductivity module of the EPW code, and HM and HP tested and expanded this module. CH and ERM supervised this project. All authors participated in the discussions and revised the manuscript.

COMPETING INTERESTS

The authors declare no competing interests.

REFERENCES

* These authors contributed equally
† Corresponding author: rmargine@binghamton.edu
‡ Corresponding author: christoph.heil@tugraz.at

[1] B. Lilia, R. Hennig, P. Hirschfeld, G. Profeta, A. Sanna, E. Zurek, W. E. Pickett, M. Amsler, R. Dias, M. I. Eremets, C. Heil, R. J. Hemley, H. Liu, Y. Ma, C. Pierleoni, A. N. Kolmogorov, N. Rybin, D. Novoselov, V. Anisimov, A. R. Oganov, C. J. Pickard, T. Bi, R. Arita, I. Errea, C. Pellegrini, R. Requist, E. K. U. Gross, E. R. Margine, S. R. Xie, Y. Quan, A. Hire, L. Fanfarillo, G. R. Stewart, J. J. Hamlin, V. Stanev, R. S. Gonnelli, E. Piatti, D. Romanin, D. Daghero, and R. Valenti, The 2021 room-temperature superconductivity roadmap, Journal of Physics: Condensed Matter **34**, 183002 (2022).

[2] J. Bardeen, L. N. Cooper, and J. R. Schrieffer, Theory of superconductivity, Phys. Rev. **108**, 1175 (1957).

[3] F. Giustino, Electron-phonon interactions from first principles, Rev. Mod. Phys. **89**, 015003 (2017).

[4] L. N. Oliveira, E. K. U. Gross, and W. Kohn, Density-functional theory for superconductors, Phys. Rev. Lett. **60**, 2430 (1988).

[5] M. Lüders, M. A. L. Marques, N. N. Lathiotakis, A. Floris, G. Profeta, L. Fast, A. Continenza, S. Massidda, and E. K. U. Gross, Ab initio theory of superconductivity. I. Density functional formalism and approximate functionals, Phys. Rev. B **72**, 024545 (2005).

[6] M. A. L. Marques, M. Lüders, N. N. Lathiotakis, G. Profeta, A. Floris, L. Fast, A. Continenza, E. K. U. Gross, and S. Massidda, Ab initio theory of superconductivity. II. Application to elemental metals, Phys. Rev. B **72**, 024546 (2005).

[7] A. Migdal, Interaction between electrons and lattice vibrations in a normal metal, Sov. Phys.-JETP **34**, 996 (1958).

[8] G. Eliashberg, Interactions between electrons and lattice vibrations in a superconductor, Sov. Phys.-JETP **11**, 696 (1960).

[9] J. Kortus, I. I. Mazin, K. D. Belashchenko, V. P. Antropov, and L. L. Boyer, Superconductivity of metallic boron in MgB$_2$, Phys. Rev. Lett. **86**, 4656 (2001).

[10] H. J. Choi, D. Roundy, H. Sun, M. L. Cohen, and S. G. Louie, The origin of the anomalous superconducting properties of MgB$_2$, Nature **418**, 758 (2002).

[11] H. J. Choi, M. L. Cohen, and S. G. Louie, Anisotropic Eliashberg theory of MgB$_2$: T_c, isotope effects, superconducting energy gaps, quasiparticles, and specific heat, Physica C: Superconductivity **385**, 66 (2003).

[12] C. Heil, S. Poncé, H. Lambert, M. Schlipf, E. R. Margine, and F. Giustino, Origin of superconductivity and latent charge density wave in NbS$_2$, Phys. Rev. Lett. **119**, 087003 (2017).

[13] I. I. Mazin, Why have band theorists been so successful in explaining and predicting novel superconductors?, Journal of Physics: Condensed Matter **31**, 174001 (2019).

[14] J. A. Flores-Livas, L. Boeri, A. Sanna, G. Profeta, R. Arita, and M. Eremets, A perspective on conventional high-temperature superconductors at high pressure: Methods and materials, Physics Reports **856**, 1 (2020).

[15] C. J. Pickard, I. Errea, and M. I. Eremets, Superconducting hydrides under pressure, Annual Review of Condensed Matter Physics **11**, 57 (2020).

[16] G. Gao, L. Wang, M. Li, J. Zhang, R. T. Howie, E. Gregoryanz, V. V. Struzhkin, L. Wang, and J. S. Tse, Superconducting binary hydrides: Theoretical predictions and experimental progresses, Materials Today Physics **21**, 100546 (2021).

[17] F. Peng, Y. Sun, C. J. Pickard, R. J. Needs, Q. Wu, and Y. Ma, Hydrogen clathrate structures in rare earth hydrides at high pressures: Possible route to room-temperature superconductivity, Phys. Rev. Lett. **119**, 107001 (2017).

[18] H. Liu, I. I. Naumov, R. Hoffmann, N. Ashcroft, and R. J. Hemley, Potential high-T_c superconducting lanthanum and yttrium hydrides at high pressure, Proceedings of the National Academy of Sciences **114**, 6990 (2017).

[19] A. Drozdov, P. Kong, V. Minkov, S. Besedin, M. Kuzovnikov, S. Mozaffari, L. Balicas, F. Balakirev, D. Graf, V. Prakapenka, *et al.*, Superconductivity at 250K in lanthanum hydride under high pressures, Nature **569**, 528 (2019).

[20] H. Wang, J. S. Tse, K. Tanaka, T. Iitaka, and Y. Ma, Superductive sodalite-like clathrate calcium hydride at high pressures, Proceedings of the National Academy of Sciences **109**, 6463 (2012).

[21] P. Kong, V. S. Minkov, M. A. Kuzovnikov, A. P. Drozdov, S. P. Besedin, S. Mozaffari, L. Balicas, F. F. Balakirev, V. B. Prakapenka, S. Chariton, *et al.*, Superconductivity up to 243 K in the yttrium-hydrogen system under high pressure, Nature communications **12**, 5075 (2021).

[22] E. Snider, N. Dasenbrock-Gammon, R. McBride, X. Wang, N. Meyers, K. V. Lawler, E. Zurek, A. Salamat, and R. P. Dias, Synthesis of yttrium superhydride superconductor with a transition temperature up to 262 K by catalytic hydrogenation at high pressures, Phys. Rev. Lett. **126**, 117003 (2021).

[23] I. A. Troyan, D. V. Semenok, A. G. Kvashnin, A. V. Sadakov, O. A. Sobolevskiy, V. M. Pudalov, A. G. Ivanova, V. B. Prakapenka, E. Greenberg, A. G. Gavriliuk, I. S. Lyubutin, V. V. Struzhkin, A. Bergara, I. Errea, R. Bianco, M. Calandra, F. Mauri, L. Monacelli, R. Akashi, and A. R. Oganov, Anomalous high-temperature superconductivity in YH₆, Advanced Materials **33**, 2006832 (2021).

[24] Y. Li, J. Hao, H. Liu, J. S. Tse, Y. Wang, and Y. Ma, Pressure-stabilized superconductive yttrium hydrides, Scientific Reports **5**, 1 (2015).

[25] Z. Li, X. He, C. Zhang, X. Wang, S. Zhang, Y. Jia, S. Feng, K. Lu, J. Zhao, J. Zhang, *et al.*, Superconductivity above 200 K discovered in superhydrides of calcium, Nature communications **13**, 2863 (2022).

[26] L. Ma, K. Wang, Y. Xie, X. Yang, Y. Wang, M. Zhou, H. Liu, X. Yu, Y. Zhao, H. Wang, G. Liu, and Y. Ma, High-temperature superconducting phase in clathrate calcium hydride CaH₆ up to 215 K at a pressure of 172 GPa, Phys. Rev. Lett. **128**, 167001 (2022).

[27] Z. Zhang, T. Cui, M. J. Hutcheon, A. M. Shipley, H. Song, M. Du, V. Z. Kresin, D. Duan, C. J. Pickard, and Y. Yao, Design principles for high-temperature superconductors with a hydrogen-based alloy backbone at moderate pressure, Phys. Rev. Lett. **128**, 047001 (2022).

[28] Y. Song, J. Bi, Y. Nakamoto, K. Shimizu, H. Liu, B. Zou, G. Liu, H. Wang, and Y. Ma, Stoichiometric ternary superhydride LaBeH₈ as a new template for high-temperature superconductivity at 110 K under 80 GPa, Phys. Rev. Lett. **130**, 266001 (2023).

[29] F. Giustino, M. L. Cohen, and S. G. Louie, Electron-phonon interaction using Wannier functions, Phys. Rev. B **76**, 165108 (2007).

[30] S. Poncé, E. Margine, C. Verdi, and F. Giustino, Epw: Electron–phonon coupling, transport and superconducting properties using maximally localized Wannier functions, Computer Physics Communications **209**, 116 (2016).

[31] H. Lee, S. Poncé, K. Bushick, S. Hajinazar, J. Lafuente-Bartolome, J. Leveillee, C. Lian, J.-M. Lihm, F. Macheda, H. Mori, H. Paudyal, W. H. Sio, S. Tiwari, M. Zacharias, X. Zhang, N. Bonini, E. Kioupakis, E. R. Margine, and F. Giustino, Electron-phonon physics from first principles using the EPW code, npj Computational Materials **9**, 156 (2023).

[32] E. R. Margine and F. Giustino, Anisotropic Migdal-Eliashberg theory using Wannier functions, Phys. Rev. B **87**, 024505 (2013).

[33] N. Marzari, A. A. Mostofi, J. R. Yates, I. Souza, and D. Vanderbilt, Maximally localized Wannier functions: Theory and applications, Rev. Mod. Phys. **84**, 1419 (2012).

[34] M. Gao, Z.-Y. Lu, and T. Xiang, Prediction of phonon-mediated high-temperature superconductivity in Li₃B₄C₂, Phys. Rev. B **91**, 045132 (2015).

[35] J.-J. Zheng and E. R. Margine, Electron-phonon coupling and pairing mechanism in $\beta - Bi_2Pd$ centrosymmetric superconductor, Phys. Rev. B **95**, 014512 (2017).

[36] R. Lucrezi and C. Heil, Superconductivity and strong anharmonicity in novel Nb–S phases, Journal of Physics: Condensed Matter **33**, 174001 (2021).

[37] R. Lucrezi, S. Di Cataldo, W. von der Linden, L. Boeri, and C. Heil, In-silico synthesis of lowest-pressure high-T_c ternary superhydrides, npj Computational Materials **8**, 119 (2022).

[38] G. P. Kafle, C. R. Tomassetti, I. I. Mazin, A. N. Kolmogorov, and E. R. Margine, Ab initio study of Li-Mg-B superconductors, Phys. Rev. Mater. **6**, 084801 (2022).

[39] G. P. Kafle, C. Heil, H. Paudyal, and E. R. Margine, Electronic, vibrational, and electron–phonon coupling properties in SnSe₂ and SnS₂ under pressure, Journal of Materials Chemistry C **8**, 16404 (2020).

[40] H. Paudyal, S. Poncé, F. Giustino, and E. R. Margine, Superconducting properties of MoTe₂ from ab initio anisotropic Migdal-Eliashberg theory, Phys. Rev. B **101**, 214515 (2020).

[41] C.-S. Lian, C. Heil, X. Liu, C. Si, F. Giustino, and W. Duan, Intrinsic and doping-enhanced superconductivity in monolayer $1H-TaS_2$: Critical role of charge ordering and spin-orbit coupling, Phys. Rev. B **105**, L180505 (2022).

[42] E. R. Margine and F. Giustino, Two-gap superconductivity in heavily *n*-doped graphene: Ab initio Migdal-Eliashberg theory, Phys. Rev. B **90**, 014518 (2014).

[43] E. R. Margine, H. Lambert, and F. Giustino, Electron-phonon interaction and pairing mechanism in superconducting Ca-intercalated bilayer graphene, Scientific Reports **6**, 21414 (2016).

[44] J. Bekaert, A. Aperis, B. Partoens, P. M. Oppeneer, and M. V. Milošević, Evolution of multigap superconductivity in the atomically thin limit: Strain-enhanced three-gap superconductivity in monolayer MgB₂, Phys. Rev. B **96**, 094510 (2017).

[45] F. Zheng, X.-B. Li, P. Tan, Y. Lin, L. Xiong, X. Chen, and J. Feng, Emergent superconductivity in two-dimensional NiTe₂ crystals, Phys. Rev. B **101**, 100505 (2020).

[46] M. Petrov, J. Bekaert, and M. V. Milošević, Superconductivity in gallenene, 2D Materials **8**, 035056 (2021).

[47] W. E. Pickett, Generalization of the theory of the electron-phonon interaction: Thermodynamic formulation of superconducting- and normal-state properties, Phys. Rev. B **26**, 1186 (1982).

[48] W. Sano, T. Koretsune, T. Tadano, R. Akashi, and R. Arita, Effect of Van Hove singularities on high-T_c superconductivity in H_3S, Phys. Rev. B **93**, 094525 (2016).

[49] D. Duan, Y. Liu, F. Tian, D. Li, X. Huang, Z. Zhao, H. Yu, B. Liu, W. Tian, and T. Cui, Pressure-induced metallization of dense $(H_2S)2H_2$ with high-T_c superconductivity, Scientific reports **4**, 6968 (2014).

[50] A. Drozdov, M. Eremets, I. Troyan, V. Ksenofontov, and S. I. Shylin, Conventional superconductivity at 203 kelvin at high pressures in the sulfur hydride system, Nature **525**, 73 (2015).

[51] M. Somayazulu, M. Ahart, A. K. Mishra, Z. M. Geballe, M. Baldini, Y. Meng, V. V. Struzhkin, and R. J. Hemley, Evidence for superconductivity above 260 K in lanthanum superhydride at megabar pressures, Phys. Rev. Lett. **122**, 027001 (2019).

[52] A. Durajski, R. Szczęśniak, and L. Pietronero, High-temperature study of superconducting hydrogen and deuterium sulfide, Annalen der Physik **528**, 358 (2016).

[53] M. Einaga, M. Sakata, T. Ishikawa, K. Shimizu, M. I. Eremets, A. P. Drozdov, I. A. Troyan, N. Hirao, and Y. Ohishi, Crystal structure of the superconducting phase of sulfur hydride, Nature physics **12**, 835 (2016).

[54] F. Capitani, B. Langerome, J.-B. Brubach, P. Roy, A. Drozdov, M. Eremets, E. Nicol, J. Carbotte, and T. Timusk, Spectroscopic evidence of a new energy scale for superconductivity in H_3S, Nature physics **13**, 859 (2017).

[55] A. F. Goncharov, S. S. Lobanov, V. B. Prakapenka, and E. Greenberg, Stable high-pressure phases in the H-S system determined by chemically reacting hydrogen and sulfur, Phys. Rev. B **95**, 140101 (2017).

[56] H. Nakao, M. Einaga, M. Sakata, M. Kitagaki, K. Shimizu, S. Kawaguchi, N. Hirao, and Y. Ohishi, Superconductivity of pure H_3S synthesized from elemental sulfur and hydrogen, Journal of the Physical Society of Japan **88**, 123701 (2019).

[57] S. Mozaffari, D. Sun, V. S. Minkov, A. P. Drozdov, D. Knyazev, J. B. Betts, M. Einaga, K. Shimizu, M. I. Eremets, L. Balicas, *et al.*, Superconducting phase diagram of H_3S under high magnetic fields, Nature Communications **10**, 2522 (2019).

[58] E. J. Pace, X.-D. Liu, P. Dalladay-Simpson, J. Binns, M. Peña Alvarez, J. P. Attfield, R. T. Howie, and E. Gregoryanz, Properties and phase diagram of $(H_2S)_2H_2$, Phys. Rev. B **101**, 174511 (2020).

[59] V. S. Minkov, V. B. Prakapenka, E. Greenberg, and M. I. Eremets, A boosted critical temperature of 166 K in superconducting d3s synthesized from elemental sulfur and hydrogen, Angewandte Chemie International Edition **59**, 18970 (2020).

[60] C. Heil, S. di Cataldo, G. B. Bachelet, and L. Boeri, Superconductivity in sodalite-like yttrium hydride clathrates, Phys. Rev. B **99**, 220502 (2019).

[61] Z. Shao, D. Duan, Y. Ma, H. Yu, H. Song, H. Xie, D. Li, F. Tian, B. Liu, and T. Cui, Unique phase diagram and superconductivity of calcium hydrides at high pressures, Inorganic chemistry **58**, 2558 (2019).

[62] S. Di Cataldo, W. von der Linden, and L. Boeri, First-principles search of hot superconductivity in La-X-H ternary hydrides, npj Computational Materials **8**, 2 (2022).

[63] S. Di Cataldo, C. Heil, W. von der Linden, and L. Boeri, $Labh_8$: Towards high-T_c low-pressure superconductivity in ternary superhydrides, Phys. Rev. B **104**, L020511 (2021).

[64] P. P. Ferreira, L. J. Conway, A. Cucciari, S. Di Cataldo, F. Giannessi, E. Kogler, L. T. F. Eleno, C. J. Pickard, C. Heil, and L. Boeri, Search for ambient superconductivity in the Lu-N-H system, Nature Communications **14**, 5367 (2023).

[65] W. L. McMillan, Transition temperature of strong-coupled superconductors, Phys. Rev. **167**, 331 (1968).

[66] P. B. Allen and R. C. Dynes, Transition temperature of strong-coupled superconductors reanalyzed, Phys. Rev. B **12**, 905 (1975).

[67] S. Xie, Y. Quan, A. Hire, B. Deng, J. DeStefano, I. Salinas, U. Shah, L. Fanfarillo, J. Lim, J. Kim, *et al.*, Machine learning of superconducting critical temperature from Eliashberg theory, npj Computational Materials **8**, 14 (2022).

[68] I. Errea, M. Calandra, C. J. Pickard, J. R. Nelson, R. J. Needs, Y. Li, H. Liu, Y. Zhang, Y. Ma, and F. Mauri, Quantum hydrogen-bond symmetrization in the superconducting hydrogen sulfide system, Nature **532**, 81 (2016).

[69] I. Errea, F. Belli, L. Monacelli, A. Sanna, T. Koretsune, T. Tadano, R. Bianco, M. Calandra, R. Arita, F. Mauri, and J. A. Flores-Livas, Quantum crystal structure in the 250-kelvin superconducting lanthanum hydride, Nature **578**, 66 (2020).

[70] R. Lucrezi, E. Kogler, S. Di Cataldo, M. Aichhorn, L. Boeri, and C. Heil, Quantum lattice dynamics and their importance in ternary superhydride clathrates, Communications Physics **6**, 298 (2023).

[71] J. A. Flores-Livas, A. Sanna, and E. Gross, High temperature superconductivity in sulfur and selenium hydrides at high pressure, The European Physical Journal B **89**, 1 (2016).

[72] A. Sanna, J. A. Flores-Livas, A. Davydov, G. Profeta, K. Dewhurst, S. Sharma, and E. K. U. Gross, Ab initio Eliashberg theory: Making genuine predictions of superconducting features, Journal of the Physical Society of Japan **87**, 041012 (2018).

[73] Y. Quan and W. E. Pickett, Van hove singularities and spectral smearing in high-temperature superconducting H_3S, Phys. Rev. B **93**, 104526 (2016).

[74] T. Jarlborg and A. Bianconi, Breakdown of the Migdal approximation at Lifshitz transitions with giant zero-point motion in the H_3S superconductor, Scientific reports **6**, 1 (2016).

[75] S. Villa-Cortés and O. De la Peña-Seaman, Effect of van hove singularity on the isotope effect and critical temperature of H_3S hydride superconductor as a function of pressure, Journal of Physics and Chemistry of Solids **161**, 110451 (2022).

[76] R. Lucrezi, P. P. Ferreira, M. Aichhorn, and C. Heil, Temperature and quantum anharmonic lattice effects on stability and superconductivity in lutetium trihydride, Nature Communications **15**, 441 (2024).

[77] J. S. Kim, L. Boeri, J. R. O'Brien, F. S. Razavi, and R. K. Kremer, Superconductivity in heavy alkaline-earth intercalated graphites, Phys. Rev. Lett. **99**, 027001 (2007).

[78] D. Yazici, K. Huang, B. D. White, I. Jeon, V. W. Burnett, A. J. Friedman, I. K. Lum, M. Nallaiyan, S. Spagna, and M. B. Maple, Superconductivity induced by electron doping in $La_{1-x}M_x OBiS_2$ ($M=$ Ti, Zr, Hf, Th), Phys. Rev. B **87**, 174512 (2013).

[79] A. Bhattacharyya, P. P. Ferreira, K. Panda, S. H. Masunaga, L. R. de Faria, L. E. Correa, F. B. Santos, D. T. Adroja, K. Yokoyama, T. T. Dorini, R. F. Jardim, L. T. F. Eleno, and A. J. S. Machado, Electron–phonon superconductivity in C-doped topological nodal-line semimetal Zr_5Pt_3: a muon spin rotation and relaxation (μSR) study, Journal of Physics: Con-

densed Matter **34**, 035602 (2021).

[80] L. E. Correa, P. P. Ferreira, L. R. de Faria, V. M. Fim, M. S. da Luz, M. S. Torikachvili, C. Heil, L. T. Eleno, and A. J. Machado, Superconductivity in Te-deficient ZrTe$_2$, The Journal of Physical Chemistry C **127**, 5162 (2023).

[81] Y. Sun, J. Lv, Y. Xie, H. Liu, and Y. Ma, Route to a superconducting phase above room temperature in electron-doped hydride compounds under high pressure, Phys. Rev. Lett. **123**, 097001 (2019).

[82] M. A. Olea-Amezcua, O. De la Peña Seaman, and R. Heid, Superconductivity by doping in alkali-metal hydrides without applied pressure: An ab initio study, Phys. Rev. B **99**, 214504 (2019).

[83] H. Guan, Y. Sun, and H. Liu, Superconductivity of H$_3$S doped with light elements, Phys. Rev. Res. **3**, 043102 (2021).

[84] T. Wang, J. A. Flores-Livas, T. Nomoto, Y. Ma, T. Koretsune, and R. Arita, Optimal alloying in hydrides: Reaching room-temperature superconductivity in LaH$_{10}$, Phys. Rev. B **105**, 174516 (2022).

[85] Y. Ge, F. Zhang, and R. J. Hemley, Room-temperature superconductivity in boron- and nitrogen-doped lanthanum superhydride, Phys. Rev. B **104**, 214505 (2021).

[86] S. Di Cataldo and L. Boeri, Metal borohydrides as ambient-pressure high-T_c superconductors, Phys. Rev. B **107**, L060501 (2023).

[87] N. Dasenbrock-Gammon, E. Snider, R. McBride, H. Pasan, D. Durkee, N. Khalvashi-Sutter, S. Munasinghe, S. E. Dissanayake, K. V. Lawler, A. Salamat, *et al.*, Evidence of near-ambient superconductivity in a N-doped lutetium hydride, Nature **615**, 244 (2023).

[88] W. Cui, T. Bi, J. Shi, Y. Li, H. Liu, E. Zurek, and R. J. Hemley, Route to high-T_c superconductivity via CH$_4$-intercalated H$_3$S hydride perovskites, Phys. Rev. B **101**, 134504 (2020).

[89] Y. Sun, Y. Tian, B. Jiang, X. Li, H. Li, T. Iitaka, X. Zhong, and Y. Xie, Computational discovery of a dynamically stable cubic SH$_3$-like high-temperature superconductor at 100 GPa via CH$_4$ intercalation, Phys. Rev. B **101**, 174102 (2020).

[90] Y. Ge, F. Zhang, R. P. Dias, R. J. Hemley, and Y. Yao, Hole-doped room-temperature superconductivity in H$_3$S$_{1-x}$Z$_x$ (Z=C, Si), Materials Today Physics **15**, 100330 (2020).

[91] A. Nakanishi, T. Ishikawa, and K. Shimizu, First-principles study on superconductivity of P- and Cl-doped H$_3$S, Journal of the Physical Society of Japan **87**, 124711 (2018).

[92] Y. Ge, F. Zhang, and Y. Yao, First-principles demonstration of superconductivity at 280 K in hydrogen sulfide with low phosphorus substitution, Phys. Rev. B **93**, 224513 (2016).

[93] Z. Shao, H. Song, H. Yu, and D. Duan, Ab initio investigation on the doped H$_3$S by V, VI, and VII group elements under high pressure, Journal of Superconductivity and Novel Magnetism **35**, 979 (2022).

[94] C. Heil and L. Boeri, Influence of bonding on superconductivity in high-pressure hydrides, Phys. Rev. B **92**, 060508 (2015).

[95] F. Fan, D. Papaconstantopoulos, M. Mehl, and B. Klein, High-temperature superconductivity at high pressures for H$_3$Si$_x$P$_{1-x}$, H$_3$P$_x$S$_{1-x}$, and H$_3$Cl$_x$S$_{1-x}$, Journal of Physics and Chemistry of Solids **99**, 105 (2016).

[96] S. Villa-Cortés and O. De la Peña-Seaman, Superconductivity on ScH$_3$ and YH$_3$ hydrides: Effects of applied pressure in combination with electron- and hole-doping on the electron–phonon coupling properties, Chinese Journal of Physics **77**, 2333 (2022).

[97] S. Villa-Cortés, M. A. Olea-Amezcua, and O. D. la Peña-Seaman, A first-principles study of theoretical superconductivity on RbH by doping without applied pressure, Journal of

[98] Y.-J. Feng, M.-J. Jiang, H.-B. Ding, H.-L. Tian, Z.-H. Lu, G.-H. Zhong, C.-L. Yang, X.-J. Chen, and H.-Q. Lin, High-temperature superconductivity in H$_3$S up to 253 K at a pressure of 140 GPa by doping holes, The Journal of Physical Chemistry C **126**, 20702 (2022).

[99] B. Liu, W. Cui, J. Shi, L. Zhu, J. Chen, S. Lin, R. Su, J. Ma, K. Yang, M. Xu, J. Hao, A. P. Durajski, J. Qi, Y. Li, and Y. Li, Effect of covalent bonding on the superconducting critical temperature of the H-S-Se system, Phys. Rev. B **98**, 174101 (2018).

[100] D. Li, Y. Liu, F.-B. Tian, S.-L. Wei, Z. Liu, D.-F. Duan, B.-B. Liu, and T. Cui, Pressure-induced superconducting ternary hydride H$_3$SXe: A theoretical investigation, Frontiers of Physics **13**, 1 (2018).

[101] E. Snider, N. Dasenbrock-Gammon, R. McBride, M. Debessai, H. Vindana, K. Vencatasamy, K. V. Lawler, A. Salamat, and R. P. Dias, Room-temperature superconductivity in a carbonaceous sulfur hydride, Nature **586**, 373 (2020).

[102] Y. Hou, B. Li, Y. Bai, X. Hao, Y. Yang, F. Chi, S. Liu, J. Cheng, and Z. Shi, Superconductivity in CeBeH$_8$ and CeBH$_8$ at moderate pressures, Journal of Physics: Condensed Matter **34**, 505403 (2022).

[103] C. Wang, S. Liu, H. Jeon, S. Yi, Y. Bang, and J.-H. Cho, Effect of hole doping on superconductivity in compressed CeH$_9$ at high pressures, Phys. Rev. B **104**, L020504 (2021).

[104] A. P. Durajski and R. Szczesniak, First-principles estimation of low-pressure superconductivity in KC$_2$H$_8$ ternary hydride, physica status solidi (RRL) – Rapid Research Letters **17**, 2300043 (2023).

[105] Q. Jiang, D. Duan, H. Song, Z. Zhang, Z. Huo, T. Cui, and Y. Yao, Room temperature superconductivity in ScH$_{12}$ with quasi-atomic hydrogen below megabar pressure, arXiv preprint arXiv:2302.02621 10.48550/arXiv.2302.02621 (2023).

[106] H. Song, Z. Zhang, T. Cui, C. J. Pickard, V. Z. Kresin, and D. Duan, High tc superconductivity in heavy rare earth hydrides, Chinese Physics Letters **38**, 107401 (2021).

[107] X. Zhong, Y. Sun, T. Iitaka, M. Xu, H. Liu, R. J. Hemley, C. Chen, and Y. Ma, Prediction of above-room-temperature superconductivity in lanthanide/actinide extreme superhydrides, Journal of the American Chemical Society **144**, 13394 (2022).

[108] S. Di Cataldo, P. Worm, L. Si, and K. Held, Absence of electron-phonon-mediated superconductivity in hydrogen-intercalated nickelates, Phys. Rev. B **108**, 174512 (2023).

[109] T. Ma, Z. Zhang, M. Du, Z. Huo, W. Chen, F. Tian, D. Duan, and T. Cui, High-throughput calculation for superconductivity of sodalite-like clathrate ternary hydrides MXH$_{12}$ at high pressure, Materials Today Physics , 101233 (2023).

[110] P. P. Ferreira, F. B. Santos, A. J. S. Machado, H. M. Petrilli, and L. T. F. Eleno, Insights into the unconventional superconductivity in HfV$_2$Ga$_4$ and ScV$_2$Ga$_4$ from first-principles electronic-structure calculations, Phys. Rev. B **98**, 045126 (2018).

[111] X. Liu, X. Huang, P. Song, C. Wang, L. Zhang, P. Lv, L. Liu, W. Zhang, J.-H. Cho, and Y. Jia, Strong electron-phonon coupling superconductivity in compressed $\alpha-$MoB$_2$ induced by double van hove singularities, Phys. Rev. B **106**, 064507 (2022).

[112] T.-T. Gai, P.-J. Guo, H.-C. Yang, Y. Gao, M. Gao, and Z.-Y. Lu, Van hove singularity induced phonon-mediated superconductivity above 77 K in hole-doped SrB$_3$C$_3$, Phys. Rev. B **105**, 224514 (2022).

[113] H.-B. Ding, Y.-J. Feng, M.-J. Jiang, H.-L. Tian, G.-H. Zhong, C.-L. Yang, X.-J. Chen, and H.-Q. Lin, Ambient-pressure high-T_c superconductivity in doped boron-nitrogen clathrates La(BN)$_5$ and Y(BN)$_5$, Phys. Rev. B **106**, 104508 (2022).

[114] J. Bekaert, C. Sevik, and M. V. Milosevic, Enhancing superconductivity in MXenes through hydrogenation, Nanoscale **14**, 9918 (2022).

[115] C. Sevik, J. Bekaert, and M. V. Milosevic, Superconductivity in functionalized niobium-carbide mxenes, Nanoscale **15**, 8792 (2023).

[116] C.-M. Hao, X. Li, A. R. Oganov, J. Hou, S. Ding, Y. Ge, L. Wang, X. Dong, H.-T. Wang, G. Yang, X.-F. Zhou, and Y. Tian, Superconductivity in compounds of sodium-intercalated graphite, Phys. Rev. B **108**, 214507 (2023).

[117] C. Liu, I. Errea, C. Ding, C. Pickard, L. J. Conway, B. Monserrat, Y.-W. Fang, Q. Lu, J. Sun, J. Boronat, *et al.*, Excitonic insulator to superconductor phase transition in ultra-compressed helium, Nature Communications **14**, 4458 (2023).

[118] Y. Luo, Y. Han, J. Liu, H. Chen, Z. Huang, L. Huai, H. Li, B. Wang, J. Shen, S. Ding, *et al.*, A unique van hove singularity in kagome superconductor CsV$_{3-x}$Ta$_x$Sb$_5$ with enhanced superconductivity, Nature Communications **14**, 3819 (2023).

[119] G. Eliashberg, Temperature Green's function for electrons in a superconductor, Sov. Phys.-JETP **12**, 1000 (1961).

[120] L. P. Gor'kov, Microscopic derivation of the Ginzburg-Landau equations in the theory of superconductivity, Sov. Phys.-JETP **7**, 505 (1958).

[121] Y. Nambu, Quasi-particles and gauge invariance in the theory of superconductivity, Phys. Rev. **117**, 648 (1960).

[122] J. W. Garland, Band-structure effects in superconductivity. I. formalism, Phys. Rev. **153**, 460 (1967).

[123] P. B. Allen and B. Mitrović, Theory of superconducting T_c (Academic Press, 1983) pp. 1–92.

[124] J. P. Carbotte, Properties of boson-exchange superconductors, Rev. Mod. Phys. **62**, 1027 (1990).

[125] L. Hedin, New method for calculating the one-particle green's function with application to the electron-gas problem, Phys. Rev. **139**, A796 (1965).

[126] M. S. Hybertsen and S. G. Louie, Electron correlation in semiconductors and insulators: Band gaps and quasiparticle energies, Phys. Rev. B **34**, 5390 (1986).

[127] F. Marsiglio and J. P. Carbotte, *Superconductivity: Conventional and Unconventional Superconductors*, edited by K. H. Bennemann and J. B. Ketterson (Springer Berlin Heidelberg, 2008) pp. 73–162.

[128] A. A. Abrikosov, L. P. Gorkov, and I. E. Dzyaloshinski, *Methods of Quantum Field Theory in Statistical Physics* (Prentice-Hall, Inc, Englewood Cliffs, NJ, 1963).

[129] F. Schrodi, A. Aperis, and P. M. Oppeneer, Increased performance of matsubara space calculations: A case study within Eliashberg theory, Phys. Rev. B **99**, 184508 (2019).

[130] H. Vidberg and J. Serene, Solving the Eliashberg equations by means of N-point Padé approximants, J. Low Temp. Phys **29**, 179–192 (1977).

[131] C. Leavens and D. Ritchie, Extension of the N-point Padé approximants solution of the Eliashberg equations to $T \sim T_c$, Solid State Communications **53**, 137 (1985).

[132] A. Davydov, A. Sanna, C. Pellegrini, J. K. Dewhurst, S. Sharma, and E. K. U. Gross, Ab initio theory of plasmonic superconductivity within the Eliashberg and density-functional formalisms, Phys. Rev. B **102**, 214508 (2020).

[133] C. Pellegrini, R. Heid, and A. Sanna, Eliashberg theory with ab-initio coulomb interactions: a minimal numerical scheme applied to layered superconductors, Journal of Physics: Materials **5**, 024007 (2022).

[134] P. Morel and P. W. Anderson, Calculation of the superconducting state parameters with retarded electron-phonon interaction, Phys. Rev. **125**, 1263 (1962).

[135] D. J. Scalapino, J. R. Schrieffer, and J. W. Wilkins, Strong-coupling superconductivity. I, Phys. Rev. **148**, 263 (1966).

[136] D. J. Scalapino, *Superconductivity* (edited by R. D. Parks, vol. 1 Dekker, New York, 1969) p. p.449.

[137] P. B. Allen, Fermi-surface harmonics: A general method for nonspherical problems. application to Boltzmann and Eliashberg equations, Phys. Rev. B **13**, 1416 (1976).

[138] F. Marsiglio, Eliashberg theory: A short review, Annals of Physics **417**, 168102 (2020).

[139] W. Kohn and L. J. Sham, Self-consistent equations including exchange and correlation effects, Phys. Rev. **140**, A1133 (1965).

[140] P. Hohenberg and W. Kohn, Inhomogeneous electron gas, Phys. Rev. **136**, B864 (1964).

[141] P. Giannozzi, S. Baroni, N. Bonini, M. Calandra, R. Car, C. Cavazzoni, D. Ceresoli, G. L. Chiarotti, M. Cococcioni, I. Dabo, *et al.*, Quantum espresso: a modular and open-source software project for quantum simulations of materials, Journal of physics: Condensed matter **21**, 395502 (2009).

[142] P. Giannozzi, O. Andreussi, T. Brumme, O. Bunau, M. B. Nardelli, M. Calandra, R. Car, C. Cavazzoni, D. Ceresoli, M. Cococcioni, *et al.*, Advanced capabilities for materials modelling with quantum espresso, Journal of physics: Condensed matter **29**, 465901 (2017).

[143] P. Giannozzi, O. Baseggio, P. Bonfà, D. Brunato, R. Car, I. Carnimeo, C. Cavazzoni, S. de Gironcoli, P. Delugas, F. Ferrari Ruffino, A. Ferretti, N. Marzari, I. Timrov, A. Urru, and S. Baroni, Quantum ESPRESSO toward the exascale, The Journal of Chemical Physics **152**, 154105 (2020).

[144] J. P. Perdew, K. Burke, and M. Ernzerhof, Generalized gradient approximation made simple, Phys. Rev. Lett. **77**, 3865 (1996).

[145] D. R. Hamann, Optimized norm-conserving vanderbilt pseudopotentials, Phys. Rev. B **88**, 085117 (2013).

[146] M. Schlipf and F. Gygi, Optimization algorithm for the generation of oncv pseudopotentials, Computer Physics Communications **196**, 36 (2015).

[147] H. J. Monkhorst and J. D. Pack, Special points for brillouin-zone integrations, Phys. Rev. B **13**, 5188 (1976).

[148] M. Methfessel and A. T. Paxton, High-precision sampling for brillouin-zone integration in metals, Phys. Rev. B **40**, 3616 (1989).

[149] S. Baroni, S. de Gironcoli, A. Dal Corso, and P. Giannozzi, Phonons and related crystal properties from density-functional perturbation theory, Rev. Mod. Phys. **73**, 515 (2001).

[150] G. Pizzi, V. Vitale, R. Arita, S. Blügel, F. Freimuth, G. Géranton, M. Gibertini, D. Gresch, C. Johnson, T. Koretsune, J. Ibañez-Azpiroz, H. Lee, J.-M. Lihm, D. Marchand, A. Marrazzo, Y. Mokrousov, J. I. Mustafa, Y. Nohara, Y. Nomura, L. Paulatto, S. Poncé, T. Ponweiser, J. Qiao, F. Thöle, S. S. Tsirkin, M. Wierzbowska, N. Marzari, D. Vanderbilt, I. Souza, A. A. Mostofi, and J. R. Yates, Wannier90 as a community code: new features and applications, Journal of Physics: Condensed Matter **32**, 165902 (2020).

[151] R. Lucrezi, P. P. Ferreira, S. Hajinazar, H. Mori, H. Paudyal, E. R. Margine, and C. Heil, Full-bandwidth anisotropic Migdal-Eliashberg theory and its application to superhydrides (2023), zenodo, https://doi.org/10.5281/zenodo.10277399.